CCFE
CULHAM CENTRE FOR FUSION ENERGY

UK Atomic Energy Authority

UKAEA-CCFE-PR(19)38

Mark Fedorov, Jan S. Wrobel, Antonio Fernandez-Caballero, Krzysztof J. Kurzydlowski, Duc Nguyen-Manh

Phase stability and magnetic properties in fcc Fe-Cr-Mn-Ni alloys from first-principles modelling

Phase stability and magnetic properties in fcc Fe-Cr-Mn-Ni alloys from first-principles modelling

Mark Fedorov, Jan S. Wrobel, Antonio Fernandez-Caballero,
Krzysztof J. Kurzydlowski, Duc Nguyen-Manh

This is a preprint of a paper submitted for publication in
Physical Review B

Phase stability and magnetic properties in fcc Fe-Cr-Mn-Ni alloys from first-principles modeling

Mark Fedorov*
Faculty of Materials Science and Engineering, Warsaw University of Technology, ul. Wołoska 141, 02-507 Warsaw, Poland and CCFE, United Kingdom Atomic Energy Authority, Abingdon, OX14 3DB, United Kingdom

Jan S. Wróbel†
Faculty of Materials Science and Engineering, Warsaw University of Technology, ul. Wołoska 141, 02-507 Warsaw, Poland

Antonio Fernández-Caballero
CCFE, United Kingdom Atomic Energy Authority, Abingdon, OX14 3DB, United Kingdom and EPSRC Centre for Doctoral Training in Materials for Demanding Environments, Faculty of Science and Engineering, University of Manchester, M13 9PL Manchester, United Kingdom

Krzysztof J. Kurzydłowski
Faculty of Mechanical Engineering, Białystok University of Technology, ul. Wiejska 45C, 15-351 Białystok, Poland

Duc Nguyen-Manh‡
CCFE, United Kingdom Atomic Energy Authority, Abingdon, OX14 3DB, United Kingdom

(Dated: May 30, 2019)

Multi-component alloy Fe-Cr-Mn-Ni is a promising new candidate system not only because of its potential application as structural materials beyond conventional austenitic steels but also for fundamental physics role played by Mn element in Fe-Cr-Ni based alloys. In this work, the phase stability of magnetic face-centered cubic (fcc) Fe-Cr-Mn-Ni system in the full composition range has been studied by the means of spin-polarized Density Functional Theory (DFT) and Cluster Expansion (CE) method. A new four-component magnetic intermetallic $FeCr_2MnNi_4$ phase, which has not been described previously in the literature, is predicted as the ground state (GS) for the quaternary system. All experimental GS of underlying fcc binary and ternary subsystems have been consistently reproduced in the present CE model among which the antiferromagnetic $L1_0$ MnNi has the lowest formation enthalpy. Nickel is found to be the most influential element from the points of view of fcc stability and the average magnitudes of magnetic moments of all the elements in the alloy. Theoretical magnetic phase diagram of Fe-Cr-Mn-Ni is found to be in good agreement with available experimental results. The average magnitude of magnetic moment is increasing with volume slower in Fe-Cr-Mn-Ni than in Fe-Cr-Ni that supports the addition of Mn to the Fe-Cr-Ni alloys in order to improve the swelling resistance under irradiation. Order-disorder phase transition temperature and chemical Short-Range Order (SRO) as functions of temperature and composition have been systematically investigated with the Monte-Carlo simulations. The increase of nickel composition in the pseudobinary alloys from 0 to 50 at.% leads to the increase of order-disorder transition temperatures, which is in a variance compared to other constituent elements. Detailed analysis of the SRO shows an important role of $L1_0$ MnNi precipitates in the increase of the order-disorder transition temperature in a wide range of quaternary concentrations, including the near-equiatomic region. The contribution of configurational entropy to the free energy of alloys calculated using the matrix formulation of the CE method shows an important effect on the alloy stability mostly in the intermediate temperature range, where the order-disorder transition takes place.

PACS numbers: 81.05.Zx, 05.10.Ln, 71.15.Mb, 81.30.Bx, 75.50.Bb

I. INTRODUCTION

High Entropy Alloys (HEAs) are a relatively new group of materials, the study of which was started from the investigation of the equiatomic CoCrFeMnNi alloy by Cantor et al. in Ref.[1], which has indicated as-cast disordered single-phase fcc solid solutions with outstanding mechanical properties. Initially explained as being stabilized by high configurational entropy of mixing, HEAs have drawn attention to the central regions of the multi-component phase diagrams. HEAs are roughly described as alloys with the composition of 4 or more elements in equal or near-equal ratios of concentrations, but the definition and the formation criteria are still not formally defined[2]. The distinctive characteristic properties observed in this class of alloys are the "four core effects", empirically described by Yeh *et al.*[3,4]: severe lattice distortion, slow diffusion rate, cocktail effect and high configurational entropy. The combination of these effects is thought to be the cause of the formation of single-phase disordered solid solutions with very unique properties.

Currently, many groups of HEAs are being studied,

showing better properties than conventional materials in their groups, such as, but not limited to[5]: refractory HEAs (such as the NbMoTaW), low-density HEAs (such as the $Li_{20}Mg_{10}Al_{20}Sc_{20}Ti_{30}$), ceramic HEAs, and transition metal HEAs, such as Cantor alloy, which are mainly studied because of their outstanding mechanical properties. Moreover, new methods of obtaining HEAs that retain their structures are being developed and tested[6], making steps to the industrial production and implementation of HEAs on larger scales.

In particular, HEAs have been shown to exhibit better resistance to irradiation damage compared to pure metals[7] and conventional austenitic steels[8–10]. This is attributed to their compositional complexity by authors of Refs.[9,10] and would make them good candidates for irradiation-facing materials in fusion and fission reactors. The main additional requirement is the removal of Co because it forms radioactive isotopes under irradiation. Such an alloy, with the composition $Cr_{18}Fe_{27}Mn_{27}Ni_{28}$, was investigated in the Oak Ridge National Laboratory both experimentally[8] and theoretically[11], and has shown good radiation-resistance properties.

Experimental investigations were done for various compositions of Cantor alloy and its derivatives in the as cast and annealed states. Near-equiatomic alloys with the fcc single-phase disordered solid solution structure in as-cast state include $FeNiMnCr_{18}$[12] and $Cr_{18}Fe_{27}Mn_{27}Ni_{28}$[8]. After annealing at temperatures below 973 K, the various precipitates have been reported to form in the equiatomic and near-equiatomic alloys, including Cr-rich bcc or σ phase in $Fe_{40}Mn_{28}Ni_8Cr_{24}$ (Ref.[13]) and CrMnFeCoNi (Refs.[14–17]); B2-FeCo and $L1_0$-MnNi in CrMnFeCoNi (Ref.[16]). This opens the question of the stabilization of single-phase disordered HEAs at lower temperatures to widen their application.

The properties of HEAs have been extensively studied experimentally, which has laid out a good basis for predictory and explanatory models to be built upon. Nowadays, the theoretical methods of materials investigation at atomic scales are being intensively applied to study HEAs and to help us understand the mechanisms of HEA formation and, hence, improve their design[18].

In order to explain the physical background of special behavior of alloys in the Fe-Cr-Mn-Ni system the vast range of concentrations have to be studied. In this context, the goal of this work is to deepen the knowledge about the phase stability and properties of the Fe-Cr-Mn-Ni alloys and to find the optimal compositions from points of view of formation free energies, order-disorder transition temperatures and homogeneity required for application in fusion reactors and to build a basis for the investigation of point defect properties and irradiation resistance. In this paper, the choice of the appropriate computational methods in order to study the aforementioned physical properties as functions of composition is following: Density Functional Theory (DFT), Cluster Expansion (CE) and Monte Carlo (MC) simulations.

Ab initio methods are the most accurate methods to investigate the ground states of materials on the atomistic scale (including the energy, crystal lattice and magnetic configuration). The most efficient *ab initio* method is DFT, where the approximated solutions of many-body Schrodinger-like equations significantly reduces the computational costs with the insignificant loss of accuracy.

The CE method is based on the usage of extensive structural database and fitting technique for various physical properties of materials and can be applied to predict possible configurations of alloys for given composition and to model the Effective Cluster Interactions (ECIs)[19,20]. In this study, the most appropriate parameter to be fitted using CE is the enthalpy of mixing (H_{mix}). The values of H_{mix} in the whole composition range can be obtained from DFT. Finally, the ECIs from CE can be employed in the MC simulations in order to investigate the behavior of alloys at finite temperatures.

The proposed approach has been developed in Ref.[21] to investigate the finite-temperature phase stability of ternary Fe-Cr-Ni system in both bcc and fcc lattices, and was successful at reproducing the experimental Short-Range Order (SRO) parameters and Order-Disorder Transitions (ODTs) temperatures. It is worth mentioning here that the effect of valence electrons plays an important role in understanding of the phase stability of HEAs[22,23]. In particular, by extending the rigid band approximation (RBA) to the magnetic alloys[23], it is shown that the spin-polarized electronic structure calculations can provide a realistic estimate for the stability of different phases present in HEAs as a function of the number of valence electrons per atom or Valence Electrons Concentration (VEC). When the VEC exceeds 6.97, the magnetic RBA model predicts that the fcc phase would be able to form. When the VEC is less than 6.97, there are either possibilities of the bcc phase stability or the coexistence between the bcc and other complex ones including Laves or σ phase.

Using the VEC criterion, the boundaries of stability region for the fcc Fe-Cr-Mn-Ni alloy can be roughly estimated. Ni and Fe have 10 and 8 valence electrons per atom, respectively. It is well-known that Ni is a fcc-stabilizer and the Fe high-temperature phase is also the fcc in conventional austenitic steels. VEC values of Mn and Cr are 7 and 6, respectively. The VEC of the former is near to the critical value 6.97 and that of the latter is below, making Cr the fcc-destabilizer. Hence, the region of quaternary alloys, where the formation of fcc phase is possible, is indicated by the maximal Cr concentration, which in the case of the Cr-[FeMnNi] pseudobinary is equal to 58.5 at.%. The resulting region in which fcc phases may be formed still takes ∼80 % of the whole concentration range. The investigation of the fcc lattice in Fe-Cr-Mn-Ni system can therefore give the stability estimate for the major part of the system.

This paper is structured as follows. Computational methodology section (Section II) consists of Cluster Expansion formalism for quaternary alloy (II.A), formalism

for calculation of chemical Short-Range Order parameters (II.B), approximations of cluster variation method for the calculation of configurational entropy (II.C) and computational details for different methods in calculations (II.D). Phase stability at T =0 K based on DFT calculations results is presented in the Section III for all subsystems of Fe-Cr-Mn-Ni quaternary, namely: binding energy studies for pure elements and motivation for the choice of representative structures (III.A); enthalpies of mixing, enthalpies of formation, volume per atom and magnetic properties for the Mn-containing binary (III.B) and ternary (III.C) subsystems, and for the quaternary system (III.D) as well as the magnetic phase diagram, table of alloy ground states and the ECIs for quaternary system and all underlying subsystems. Finite temperature phase stability analysis is presented in Section IV and includes the results for a configurational entropy from a combined Monte Carlo and Cluster Expansion method (IV.A) and it's contribution to the free energy of mixing (IV.B), the order-disorder transition temperatures (IV.C) and Short-Range Order parameters (IV.D) studied in the whole concentration range. The main results of current work are summarized in the Conclusions section.

II. COMPUTATIONAL METHODOLOGY

A. Cluster Expansion Formalism for Quaternary Alloy

The enthalpy of mixing of an alloy with chosen configuration represented by a vector of configurational variables $\vec{\sigma}$ can be calculated from DFT using the value of total energy per atom of simulated alloy structure $E_{tot}^{lat}(\vec{\sigma})$ and the corresponding pure elements $E_{tot}^{lat}(p)$ underlying the same lattice as the alloy structure as follows:

$$\Delta H_{mix}(\vec{\sigma}) = E_{tot}^{lat}(\vec{\sigma}) - \sum_{p=1}^{K} c_p E_{tot}^{lat}(p), \tag{1}$$

where K is the number of alloy components and c_p are the average concentrations of each alloy component.

In the cluster expansion formalism, the enthalpy of mixing can be parametrized as a polynomial in the occupational variables[24]:

$$\Delta H_{mix}(\vec{\sigma}) = \sum_{\omega,n,s} J_{\omega,n}^{(s)} m_{\omega,n}^{(s)} \langle \Gamma_{\omega',n'}^{(s')}(\vec{\sigma}) \rangle_{\omega,n,s}, \tag{2}$$

where the summation is performed over all the clusters, distinct under symmetry operations in the studied lattice, represented by the following parameters: ω and n are the cluster size (the number of lattice points in the cluster) and its label (maximal distance between two atoms in the cluster in terms of coordination shells), respectively, see Fig. 1; (s) is the decoration of cluster by point function $\gamma_{j,K}(\sigma_i)$. $m_{\omega,n}^{(s)}$ denotes the site multiplicity of the decorated clusters (in per-lattice-site units); and $J_{\omega,n}^{(s)}$ represents the ECI energy corresponding to the same (s) decorated cluster.

$\langle \Gamma_{\omega',n'}^{(s')}(\vec{\sigma}) \rangle_{\omega,n,s}$ are the cluster functions, averaged over all the clusters of size ω' and label n' decorated by the sequence of point functions (s') that are equivalent by the symmetry to the cluster ω, n and decorated by the same sequence of point functions (s). Later in the text, $\langle \Gamma_{\omega',n'}^{(s')}(\vec{\sigma}) \rangle_{\omega,n,s}$ is referred to as $\langle \Gamma_{\omega,n}^{(s)}(\vec{\sigma}) \rangle$ for ease of notation. In Monte Carlo formalism, cluster functions are also averaged over the all MC steps at chosen temperature, which controls the accuracy and the computational costs of the calculations.

The definition of point functions in this work is the same as in Ref.[25] and as following:

$$\gamma_{j,K}(\sigma_i) = \begin{cases} 1 & \text{if } j = 0\ , \\ -\cos\left(2\pi \lceil \frac{j}{2} \rceil \frac{\sigma_i}{K}\right) & \text{if } j > 0 \text{ and odd}, \\ -\sin\left(2\pi \lceil \frac{j}{2} \rceil \frac{\sigma_i}{K}\right) & \text{if } j > 0 \text{ and even}, \end{cases} \tag{3}$$

where $i = 0, 1, 2, ...(K-1)$, j is the index of point functions $j = 0, 1, 2, ...(K-1)$ and $\lceil \frac{j}{2} \rceil$ stands for the ceiling function - rounding up to the closest integer.

The cluster function is then defined as the product of orthonormal point functions of occupation variables[26] $\gamma_{j,K}(\sigma_i)$, on specific cluster described by ω and n:

$$\Gamma_{\omega,n}^{(s)}(\vec{\sigma}) = \gamma_{j_1,K}(\sigma_1)\gamma_{j_2,K}(\sigma_2)\cdots\gamma_{j_\omega,K}(\sigma_\omega). \tag{4}$$

The matrix $\bar{\bar{\tau}}_K$, relating the point probabilities to the point correlation functions, can be constructed using point functions $\gamma_{j,K(\sigma_i)}$ as its elements:

$$(\bar{\bar{\tau}}_K) = \begin{pmatrix} \gamma_{j=0,K}(\sigma_i=0) & \cdots & \gamma_{j=0,K}(\sigma_i=K-1) \\ \vdots & \ddots & \vdots \\ \gamma_{j=K-1,K}(\sigma_i=0) & \cdots & \gamma_{j=K-1,K}(\sigma_i=K-1) \end{pmatrix}. \tag{5}$$

The exact $\bar{\bar{\tau}}_K$ matrices for 2-, 3-, and 4-component systems are presented in Eq. A1.

The general expression for the cluster correlation function is then may be determined using the $\bar{\bar{\tau}}_K$ matrix[26]:

$$\langle \Gamma_{\omega,n}^{(s)} \rangle = \sum_{A,B,\cdots} (\prod_{\omega} \bar{\bar{\tau}}_K)_{(s),A,B,\cdots} y_{\omega,n}^{A,B,\cdots}, \tag{6}$$

where $(\prod_{\omega} \bar{\bar{\tau}}_K)_{(s),A,B,\cdots}$ denotes the matrix direct product (Kronecker product); the summation is done over the atomic species composing the alloy; $y_n^{A,B,\cdots}$ denotes the temperature-dependent *many*-body probability of finding atomic species $A, B, \cdots$ in the corresponding ω cluster with coordination shell, denoted by n.

Using the form of Eq. (6), two-body cluster correlation function written in form[26]:

$$\langle \Gamma_{2,n}^{(s)} \rangle = \sum_{A,B} (\bar{\bar{\tau}}_K \otimes \bar{\bar{\tau}}_K)_{(s),A,B} y_{2,n}^{AB}, \tag{7}$$

where $\otimes$ denotes the matrix direct product. Accordingly, the three and four-body correlation functions within the matrix formulation are defined as:

$$\langle \Gamma^{(s)}_{3,n} \rangle = \sum_{A,B,C} (\bar{\bar{\tau}}_K \otimes \bar{\bar{\tau}}_K \otimes \bar{\bar{\tau}}_K)_{(s),A,B,C} y^{ABC}_{3,n}, \quad (8)$$

and

$$\langle \Gamma^{(s)}_{4,n} \rangle = \sum_{A,B,C,D} (\bar{\bar{\tau}}_K \otimes \bar{\bar{\tau}}_K \otimes \bar{\bar{\tau}}_K \otimes \bar{\bar{\tau}}_K)_{(s),A,B,C,D} y^{ABCD}_{4,n}, \quad (9)$$

respectively.

The 3- and 4-body probability functions can be determined by the inverse of the respective correlation functions and they are presented in Eqs. (A2) and (A3).

The complete set of decorations (s) for a cluster of size ω corresponding to the K^ω list of indices is generated by applying the permutation representation of the space group # 225 (O^5_h) elements to the decorations belonging to the cluster and its subclusters. With symmetry, all correlation functions are generated from the given symmetrically unique set of correlations for each cluster in the Hamiltonian expansion.

B. Chemical Short-Range Order Parameters

Chemical Short-Range Order (SRO) in the alloys can be analysed using the Warren-Cowley SRO parameters. They can be obtained from the relation of pair probabilities and point probabilities by using the following expression:

$$\alpha^{AB}_n = 1 - \frac{y^{AB}_{2,n}}{c_A c_B}. \quad (10)$$

The Warren-Cowley SRO parameters have been formulated in[26,27] based on the principles, that e.g. for clusters of two sites, the decorations indices can be interchanged because the space group O^5_h contains two-fold symmetry axes and translations that transform one site into the other. For clusters with more than 2 sites, the permutation operators are more complex and depend on the specific sites occupied in the clusters. For example, for the 3-body cluster labelled by $\omega = 3; n = 2$ in Fig. 1, using group theoretical arguments it can be found for a three sites cluster that the symmetrically unique decoration (131) is equivalent to the (113) i.e. $\langle \Gamma^{(131)}_{3,2} \rangle \equiv \langle \Gamma^{(113)}_{3,2} \rangle$.

The fact that the inverse of a Kronecker product of two matrices is equivalent to the product of inverse matrices can be used to express the pair probabilities in terms of pair correlations. For this, the inverse of $\bar{\bar{\tau}}_K$ matrix, $\bar{\bar{\tau}}^{-1}_K$ can be obtained with its elements defined as follows[26]:

$$(\bar{\bar{\tau}}^{-1}_K)_{ij} = \frac{1}{K} \begin{cases} 1 & \text{if } j = 0\ , \\ -2\sin\left(2\pi\lceil \frac{j}{2} \rceil \frac{\sigma_i}{K}\right) & \text{if } j > 0 \text{ and even}, \\ -2\cos\left(2\pi\lceil \frac{j}{2} \rceil \frac{\sigma_i}{K}\right) & \text{if } j > 0 \\ & \text{and } j < K-1 \\ & \text{and } j \text{ is odd}, \\ -\cos\left(2\pi\lceil \frac{j}{2} \rceil \frac{\sigma_i}{K}\right) & \text{if } j = K-1 \\ & \text{and } j \text{ is odd}. \end{cases} \quad (11)$$

The exact forms of $\bar{\bar{\tau}}^{-1}_K$ matrices for the 2-, 3- and 4-component systems in presented in Eq. A4.

Using the $\bar{\bar{\tau}}^{-1}_K$ matrix, the point probability function is written as:

$$y^A_{1,1} = \sum_s (\bar{\bar{\tau}}^{-1}_K)_{A,(s)} \langle \Gamma^{(s)}_{1,1} \rangle, \quad (12)$$

and from Eq. (7) the pair probability function is written as:

$$y^{AB}_{2,n} = \sum_s (\bar{\bar{\tau}}^{-1}_K \otimes \bar{\bar{\tau}}^{-1}_K)_{A,B,(s)} \langle \Gamma^{(s)}_{2,n} \rangle. \quad (13)$$

Since MC simulations with the Effective Cluster Interaction (ECI) from CE give an information about $\langle \Gamma^{(s)}_{2,n} \rangle$, the Warren-Cowley parameters can be easily calculated directly form MC simulations. The exact formulas for the calculation of the Warren-Cowley SRO parameters for each pair of atoms in the 4-component system, used in this work, is presented in Eq. A5, which were formulated in Ref.[27]. More explicitly, the Warren-Cowley SRO parameters can be determined in terms of correlation functions from MC simulations using the matrix formulation in Eq. 11. The explicit formula for the SRO Warren-Cowley parameters is given as:

$$\alpha^{AB}_n = 1 - \frac{\sum_s (\bar{\bar{\tau}}^{-1}_K \otimes \bar{\bar{\tau}}^{-1}_K)_{A,B,(s)} \langle \Gamma^{(s)}_{2,n} \rangle}{\left(\sum_s (\bar{\bar{\tau}}^{-1}_K)_{A,(s)} \langle \Gamma^{(s)}_{1,1} \rangle\right)\left(\sum_s (\bar{\bar{\tau}}^{-1}_K)_{B,(s)} \langle \Gamma^{(s)}_{1,1} \rangle\right)}. \quad (14)$$

C. Configurational Entropy Contribution

Free energy of mixing for the alloy is defined as follows:

$$F_{mix} = H_{mix} - TS_{mix}, \quad (15)$$

where the mixing entropy term

$$S_{mix} = S^{conf}_{mix} + S^{vib}_{mix} + S^{el}_{mix} + S^{mag}_{mix}, \quad (16)$$

consists of configurational, vibrational, electronic and magnetic mixing entropies. Relative magnitudes of the aforementioned contributions to the mixing entropy have been estimated in Refs.[2,4,28–30] to be following: $S^{conf}_{mix} >$

$S^{vib}_{mix} > S^{el}_{mix} > S^{mag}_{mix}$, and thought the maximal magnitude of S^{vib} can reach the value of 3 times larger than the maximal value of S^{conf}, the values of S^{vib}_{mix} are closer to the electronic and magnetic contributions. Hence, even though the vibrational, electronic and magnetic mixing entropies influence the stability of the alloy, the main entropic contribution to the F_{mix} comes from configurational mixing entropy.

The cluster contribution to the entropy as determined from Monte Carlo calculations of correlation functions using the approach established in Ref.[26], each cluster resulting in an entropy formula and denoted by ϵ. The generalized formula for the entropy, taking into account all *many*-body interactions is then expressed as:

$$S^{conf}_{\omega,n} = k_B \sum_q w^{\omega,n}_q \sum_s y^{(s)}_q \ln(y^{(s)}_q). \tag{17}$$

The index (s) of the inner sum runs for all possible decorations of clusters of any given cluster indexed by q, which are given by K^{ω_q} total decorations.

The weights in the sum are worked out following the iterative Barker formula[31] in the formalism of cluster variation method. Detailed derivation is formulated elsewhere[26], and the explicit values are listed in the Supplementary materials, Table SIII.

D. Computational Details

DFT calculations with collinear spin-polarization were performed using the projector augmented wave (PAW) method implemented in VASP[32–37]. Exchange and correlation were treated in the generalized gradient approximation GGA-PBE[38]. The core configurations of Fe, Cr, Mn and Ni in PAW potentials were [Ar]$3d^7 4s^1$, [Ar]$3d^5 4s^1$, [Ar]$3d^6 4s^1$ and [Ar]$3d^9 4s^1$, respectively.

Total energies were calculated using the Monkhorst-Pack mesh[39] of k-points in the Brillouin zone, with k-mesh spacing of 0.2 Å^{-1}. This corresponds to 12x12x12 k-point mesh for a four-atom fcc conventional unit cell. The plane wave cut-off energy used in the calculations was 400 eV. The total energy convergence criterion was set to 10^{-6} eV/cell, and force components were relaxed to 10^{-4} eV/Å.

Mapping DFT energies to CE was performed using the ATAT package[24,25,40,41]. In order to find the ECI for binary fcc alloys, the initial database of 28 structures from Ref.[42] was used. For ternary fcc alloys the initial database consisted of 98 structures adapted from Ref.[43]. The quaternary database was constructed following the approach from Ref.[21]: the ternary database was considered, the symmetry and the number of non-equivalent positions (NEPs) in each structure was checked and the structures with the number of NEPs greater than three were included in the quaternary fcc structure database by populating the higher NEPs with various combinations of elements.

Fe-Cr-Mn-Ni alloys show complex magnetic behavior even in collinear calculations with competing stability of non-magnetic (NM), ferromagnetic (FM), antiferromagnetic (AFM) and ferrimagnetic (FiM) configurations. Thus, full relaxations starting from various initial magnetic configurations were performed in order to find the most stable magnetic order characterizing a given structure.

Only the most stable magnetic configurations for each compositions have been taken into account during the construction of the data set, which later have been mapped to CE, which allowed to account for the magnetism in the implicit way. The CE routine of the ATAT code has produced the number of structures, absent in the initial data set. This helped to construct more precise concentration mesh of structures, calculated with DFT. Fitting of the final DFT structures data set to the CE produced the ECIs, which were used in the following Monte Carlo simulations.

Mapping of the mixing enthalpies of 835 structures was conducted for quaternary system and the cross-validation score of 12.95 meV was achieved. Such value of Cross-Validation Score (CVS) is considered to be reasonable taking into account the complex magnetic structure of the investigated system. The set of clusters, which have minimized the CVS, consists of 6 two-body, 2 three-body and 1 four-body undecorated clusters, illustrated in Fig. 1. In this study, the CE Hamiltonian have been constructed for the quaternary fcc Fe-Cr-Mn-Ni system as well as for the corresponding ternary and binary subsystems. For the sake of consistency, for all the systems, clusters with the same size and relative positions of points have been taken into account (see Fig. 1). Therefore, the enthalpy of mixing for all considered systems in the CE formalism can be written as:

$$\begin{aligned}\Delta H_{mix}(\vec{\sigma}) = & \sum_{\omega,n,s} J^{(s)}_{\omega,n} m^{(s)}_{\omega,n} \langle \Gamma^{(s)}_{\omega,n}(\vec{\sigma}) \rangle = \\ & = J^{(0)}_{1,1} \left\langle \Gamma^{(0)}_{1,1} \right\rangle + \sum_s J^{(s)}_{1,1} \left\langle \Gamma^{(s)}_{1,1} \right\rangle + \\ & + \sum_{\mathrm{n}=1}^{6} \sum_s m^{(s)}_{2,\mathrm{n}} J^{(s)}_{2,\mathrm{n}} \left\langle \Gamma^{(s)}_{2,\mathrm{n}} \right\rangle + \\ & + \sum_{\mathrm{n}=1}^{2} \sum_s m^{(s)}_{3,\mathrm{n}} J^{(s)}_{3,\mathrm{n}} \left\langle \Gamma^{(s)}_{3,\mathrm{n}} \right\rangle + \\ & + \sum_s m^{(s)}_{4,1} J^{(s)}_{4,1} \left\langle \Gamma^{(s)}_{4,1} \right\rangle ,\end{aligned} \tag{18}$$

where $J^{(s)}_{\omega,n}$ are different in each studied subsystem.

Size ω, label n, decoration (s), multiplicity $m^{(s)}_{\omega,n}$, coordinates of points and $J^{(s)}_{\omega,n}$ (in meV) of aforementioned clusters are listed in the Supplementary materials, Table S I.

ECIs, obtained using the structure inversion method[44], for studied binary and ternary subsystems as well as for

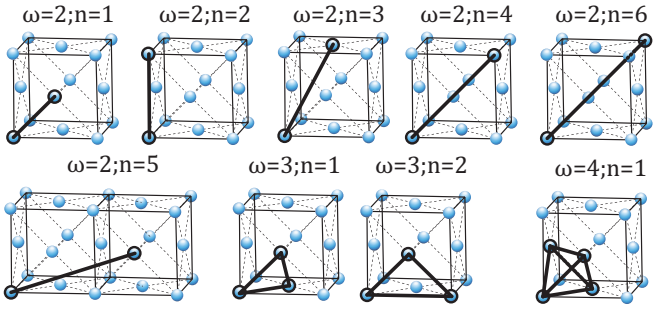

FIG. 1: Undecorated 2-, 3- and 4-body clusters $m^{(s)}_{\omega,n}$ used in this work.

quaternary system are presented in the corresponding sections.

Semi-canonical MC simulations were performed also using the ATAT package. Most of the simulations were performed using a cell containing 2048 atoms in the form of 8x8x8 fcc unit cell. For each composition, simulations were performed starting from a disordered high-temperature state at $T = 3000$ K . The alloy was then cooled down with the temperature step of $\Delta T = 100$ K, with 2000 equilibration and accumulation Monte Carlo passes. Thermodynamic Integration (TDI) calculations were performed with the temperature step of $\Delta T = 5$ K in order to obtain the accurate values of the configurational entropy.

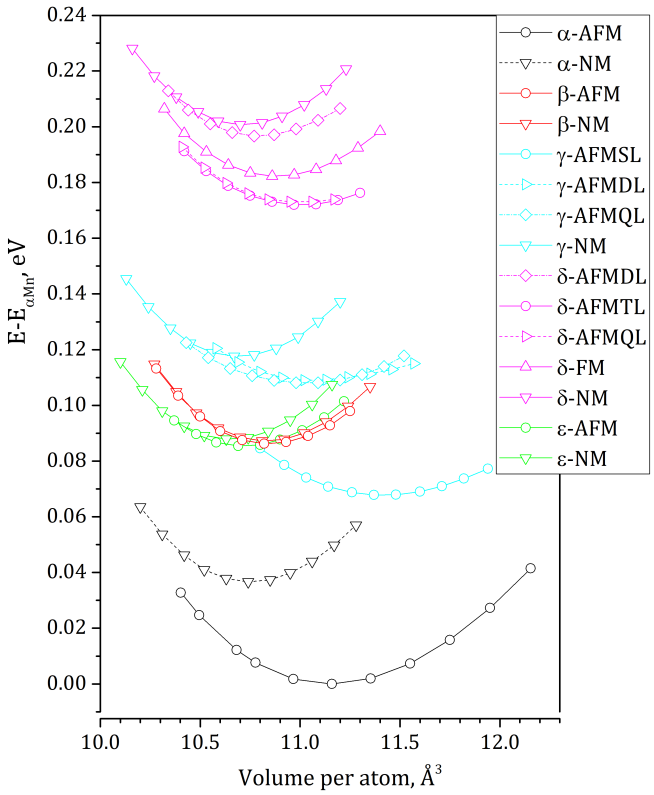

FIG. 2: Calculated equations of state for known and hypothetical crystal structures and magnetic configurations of Mn.

III. PHASE STABILITY AT 0 K

A. Pure Elements

Extensive calculations of total energy as a function of volume have been conducted for known and hypothetical crystal structures and magnetic configurations of Fe, Cr, Mn and Ni in order to understand the stability of pure elements and obtain the reference energies of the most stable magnetic configurations for the CE method.

The most stable fcc structures of pure elements from the current studies at 0 K are: AntiFerroMagnetic Double-Layer (AFMDL) Fe, Non-Magnetic (NM) Cr, FerroMagnetic (FM) Ni and AntiFerroMagnetic Single-Layer (AFMSL) Mn. Global ground states of pure elements from the current studies at 0 K are following: FM bcc Fe, AFM bcc Cr, FM fcc Ni, AFM σ-phase α-Mn.

Experimental ground states of pure elements at 0 K are: non-collinear bcc FM Fe[45], spin-density wave bcc Cr[46], FM fcc Ni[45]. Experimental results for Mn indicate both collinear and non-collinear AFM σ-phase α-Mn, as discussed further. However, the total energies per atom of collinear and non-collinear configurations obtained from DFT calculations[47] are almost indistinguishable.

Due to the reason of the time scale, the non-collinearity has not been considered in the current work, and the enthalpies of formation have been calculated with the respect to the collinear global ground states.

Binding energy curves for different Mn structures are shown in Fig. 2 with a reference to the binding energy of α-Mn GS ($E - E^{AFM}_{\alpha-Mn}$). It can be seen from Fig. 2, that lowering the volume per atoms significantly below the equilibrium volume for each structure lead the magnetic ordering to change to the non-magnetic, indicating the high-pressure magnetic phase transition. The comparison of magnetic ordering, volume per atom and the $E - E^{AFM}_{\alpha-Mn}$ values with experimental and theoretical results is presented in Table I. Magneto-volume relation for studied structural and magnetic phases of Mn with non-zero Average Magnitude of Magnetic Moments (AMMMs) is presented in Fig. 3 and it shows that the volume per atom increases with increasing AMMM in all structures.

The GS of Mn, α-Mn, has a very complex atomic structure. The lattice is identified as σ-phase with 58 atoms in the unit cell and 4 crystallographically and magnetically inequivalent sites, where the half of the atoms in each site is ordered antiferromagnetically to the other half. Table II presents the comparison of the magnitudes of magnetic moments for this sites with the previous experimental and theoretical results. It can be seen that the values obtained in this work lie within the range of

TABLE I: Magnetic ordering, AMMM (in μ_B), volume per atom (in Å^3) and $E - E^{AFM}_{\alpha-Mn}$ (in meV) for different phases of pure Mn compared to previous experimental and theoretical data.

Phase	Magnetic ordering		AMMM [μ_B]			V/at [Å^3]			$E - E^{AFM}_{\alpha-Mn}$ [meV]	
	Prev.	Present	Theor.	Exp.	Present	Theor.	Exp.	Present	Prev.	Present
α-Mn	AFM	NM			0	10.75[a]		10.74		21
		AFM		0.5[b]	0.57	11.08[c]	12.05[d]	11.13	0[c]	0
β-Mn	FiM	NM			0	12.17[e]		10.81		72
		AFM	0.5[e]		0.24	12.40[e], 10.84[c]	12.44[e,f,g]	10.82	63[c]	71
γ-Mn (fcc)	AFM	NM			0			10.67		102
		AFMSL	2.13[h]		1.84	11.16[c]	12.95[i]	11.37	67[c]	52
		AFMDL			1.28			11.02		94
		AFMQL			1.14			10.98		93
δ-Mn (bcc)	AFM	NM			0			10.70		185
		FM	0.99[h]		0.85	11.12[c]		10.86	146[c]	167
		AFMDL			0.54			10.77		181
		AFMTL			0.98			10.97		157
		AFMQL			0.78			10.95		158
ϵ-Mn (hcp)	AFM	NM			0			10.63		72
		AFM	0.20[h]		0.53	10.72[c]		10.69	61[c]	70

[a] - Hobbs *et al.*[47], [b] - Shull *et al.*[48], [c] - Hafner *et al.*[49], [d] - Lawson *et al.*[50], [e] - Asada *et al.*[51], [f] - Preston *et al.*[52], [g] - Sliwko *et al.*[53], [i] - Wyckoff *et al.*[54], [h] - Asada *et al.*[55]

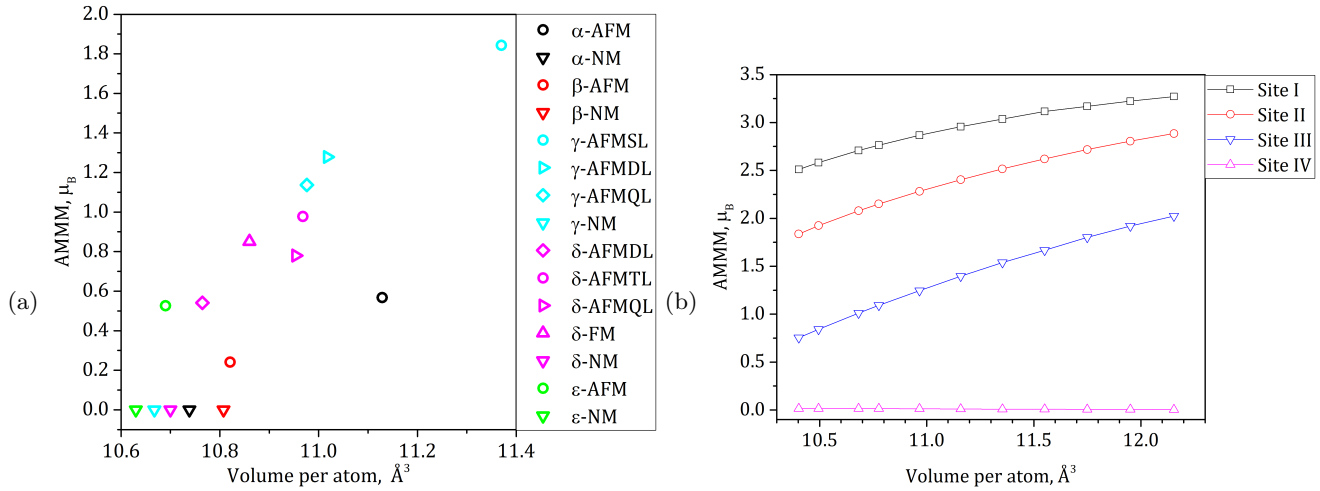

FIG. 3: Magneto-volume relation (a) for all calculated Mn structures at equilibrium volume and (b) for 4 sites in AFM α-Mn.

previous experimental and theoretical results.

Due to the fact that the ground state crystal lattices of Fe, Cr, Mn and Ni belong to different crystallographic groups, the analysis of alloy stability in Sections III.2 - III.5 have been performed both in terms of enthalpy of mixing and enthalpy of formation. Since only Ni ground state is fcc, it will act as a fcc phase stabilizer - the increase of Ni content will more likely result in the stabilization of fcc lattice structure. In contrary to Ni, Cr has the highest difference of $E_{fcc} - E_{GS} = 0.394$ eV, and therefore can inhibit a formation of fcc phase in favor of bcc phase. The values of $E_{fcc} - E_{GS}$ for Fe and Mn are 5 times smaller compared to the Cr.

B. Binary Subsystems

In this subsection, there are presented enthalpies of formation, enthalpies of mixing, volumes per atom and AMMM obtained using DFT at 0 K for the binary systems containing Mn, namely Cr-Mn, Fe-Mn and Mn-Ni. Since the methodology and the results for Fe-Cr, Cr-Ni and Fe-Ni are similar to one used in Ref.[21], they are described in the Supplementary materials, Section S I.A-C. ECIs for all binaries are also presented. A chosen set of undecorated clusters (6 two-body, 2 three-body and 1 four-body) gives for binaries the same numbers of the decorated clusters. The interpretation of ECIs is given for the first and second nearest neighbors (1NN and 2NN, respectively).

TABLE II: AMMM (in μ_B) of atoms on different sites in antiferromagnetic α-Mn structure compared to previous experimental and theoretical data.

Site	No. of atoms	Magnetic moment [μ_B]						
		Exp.[a] Col.	Exp.[b] Col.	Exp.[c] Col.1	Exp.[c] Col.2	Exp.[d] N.Col.	Theor.[e] N.Col.	Present work
I	2	1.35	1.8	1.54	2.5	2.83	3.19	2.94
II	8	1.35	1.4	1.54	2.5	1.83	2.79	2.39
III	24	0.99	1.2	3.08	1.7	0.61	1.81	1.38
IV	24	0.22	0.1	0	0	0.47	0.02	0.02

[a] - Kunitomi *et al.*[56], [b] - Oberteuffer *et al.*[57], [c] - Kasper and Roberts *et al.*[58], [d] - Lawson *et al.*[50], [e] - Hobbs *et al.*[47].

Enthalpies of formation of binary structures are calculated as the energy of the structure with respect to the energies of pure GSs, i.e. antiferromagnetic bcc-Cr, ferromagnetic bcc-Fe, antiferromagnetic α-Mn and ferromagnetic fcc-Ni. Formation energies of the most stable pure fcc states are connected by a dashed line that represents the "zero line" of mixing enthalpies of the considered systems, so all structures with energies below and above it possess negative and positive enthalpies of mixing, respectively.

The effect of magnetism on the volume of structures is analysed by comparing the calculated values of volume to the linear heuristic estimate, called the Vegard's law, in which the value of volume per atom for the mixture is equal to the sum of volumes per atom of it's constituents factoring their concentration.

The binary enthalpies of mixing from DFT calculations and CE are compared in the Supplementary materials, Fig. S 4.

1. *Cr-Mn Binary*

The final database for the CE model for fcc Cr-Mn binary consists of 55 structures and the Cross-Validation Score (CVS) between DFT and CE is equal to 8.3 meV. ECIs (Fig. 4(b)) have the smallest absolute values, compared to the other binaries. 1NN ECI is positive and 2NN ECI is negative, which means that unlike elements are attracted in 1NN and repelled in 2NN.

The ground states of Cr-Mn system in terms of mixing enthalpy are Cr_3Mn (Z1(100)) and CrMn (Z2(100)), but all fcc Cr-Mn structures exhibit positive enthalpy of formation (Fig. 5(a)). As a consequence, no stable fcc phases are observed experimentally for this system. Enthalpy of mixing shows tendency to decrease in near-equiatomic concentration region, whereas enthalpy of formation shows strong linear drop with the increase of Mn concentration.

Chromium suppresses high magnetic moment of Mn resulting in NM region with the Cr concentration larger than 50at.%, where the volumes per atom hold almost perfectly the Vegard's law for NM reference structures(Fig. 5(b)). For Cr concentration smaller than 50at.% structures are FiM and the volumes per atom lay between magnetic and non-magnetic Vegard's law estimates, where Mn dominates the magnetic structure. The value of AMMM increases with the increase of Mn concentration. The Cr-rich NM stability region and the Mn-rich FiM stability region are divided with non-magnetic CrMn structure (Fig. 5(c)).

2. *Fe-Mn Binary*

The final CE database for fcc Fe-Mn binary consists of 58 structures and CVS between DFT and CE is 11.6 meV and ECIs are given in Fig. 4(d). The 1NN ECI is positive and the 2NN ECI is negative and twice larger, which means that the unlike elements are strongly repelled in the second coordination shell and attracted in the first coordination shell - this favors the formation of $L1_2$ Fe_3Mn phase, which is the ground state of Fe-Mn system in terms of enthalpy of mixing.

The other alloy GS in terms of enthalpy of mixing are $FeMn_{31}$, $FeMn_{15}$ and Fe_3Mn_4. Trends in enthalpy of mixing (Fig. 6(a)) are consistent with previous calculations[59]. The enthalpies of formation of all Fe-Mn structures are positive, which means that at 0 K there are no stable compositions from the point of view of enthalpy of formation. However the values of enthalpies tend to decrease in near-equiatomic concentration region, which is consistent with previous calculations[60], and with previous assessments of metastability of fcc alloys[61]. This can be related to the fact that the most stable α-Mn structure has much more complex lattice in ground state than fcc, and GS of Fe is ferromagnetic bcc within collinear calculations, although it should be noted that Fe has stable fcc lattice above 1190 K, and austenite steels, which have fcc lattice, can be stablized to exist even at room temperature. The study of Fe-Mn alloy powders has shown a presence of martensite (bcc) and austenite (fcc)[62,63]. The latter is observed as a single phase in $Fe_{70}Mn_{30}$ alloy[64], which is close in a concentration to the fcc Fe_3Mn ground state.

In the Fe-Mn binary subsystem, the volumes of compositions lie between the Vegard's law estimates for magnetic and non-magnetic reference structures (Fig. 6(b)).

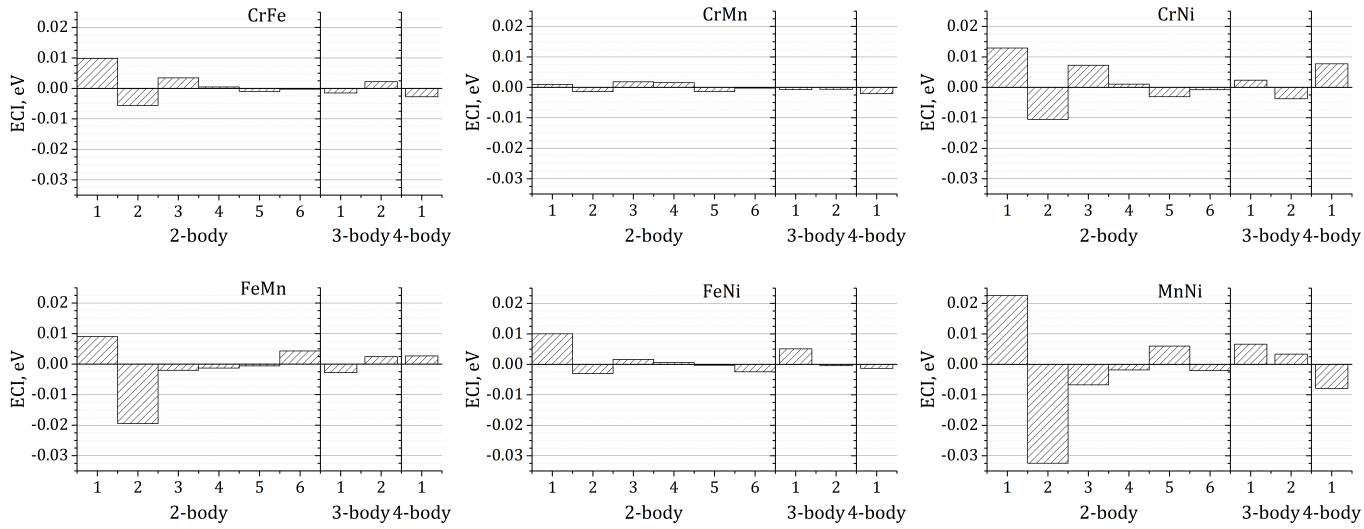

FIG. 4: ECIs for binary subsystems.

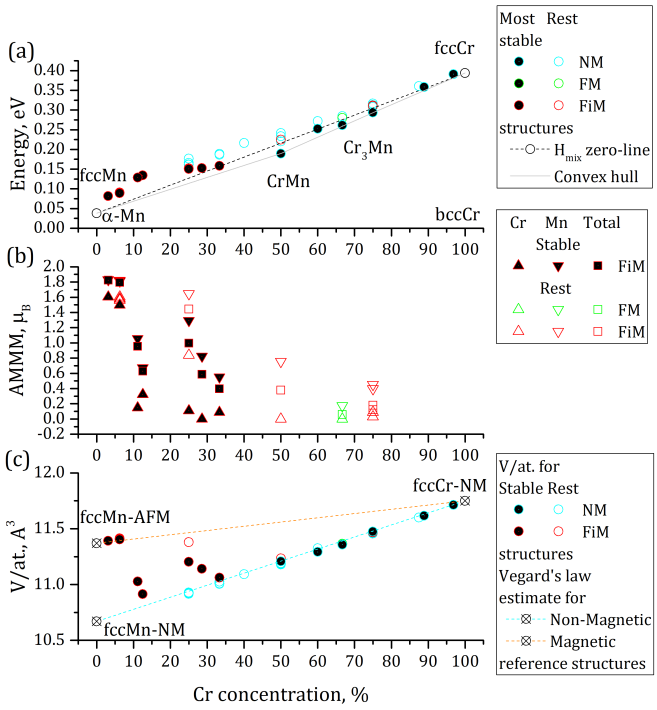

FIG. 5: (a) Enthalpy of formation, (b) average magnitudes of magnetic moments per atom, (c) volume per atom of fcc Cr-Mn structures calculated using DFT. The results obtained for the most stable structures and magnetic configurations for each considered alloy composition are indicated by filled shapes, the less stable structures are indicated by open shapes.

Fe-rich and Mn-rich structures almost perfectly satisfy the estimate for magnetic reference structures, but tend to decrease with the proximity of Fe-Mn ratio to the equiatomic composition.

The antiferromagnetism in fcc Fe-Mn alloys was experimentally observed in wide range of concentrations[65–67]. Current results show that the magnetic moments of Mn atoms are antiferromagnetic to Fe for almost all structures. AMMMs of both elements slowly decrease with increasing Mn concentration (Fig. 6(c)). AMMM for fcc $Fe_{50}Mn_{50}$ structure is 1.5 μ_B, which is close to the experimental value of 1.2 μ_B estimated for $Fe_{50}Mn_{50}$ disordered solid solution in Ref.[66]. AMMMs of the system are decreasing with increasing Mn concentration and are dominated by Fe atoms in Fe-rich region, and by Mn atoms in Mn-rich region. Average magnitudes of magnetic moment of Mn atoms vary between the value for fcc AFMSL Mn in Mn-rich region and site-I magnetic moment from α-Mn in Fe-rich region (see Table II).

3. *Mn-Ni Binary*

For the fcc Mn-Ni system, the database for the CE model consists of 52 structures and CVS between DFT and CE is 11.6 meV. ECIs (Fig. 4(f)) are the strongest among all binaries. Similarly to Fe-Mn, the 1NN ECI is positive and 2NN is 1.5 times stronger and negative, which translates into attraction of unlike atoms in 1NN and repulsion in 2NN. This favors the formation of $MnNi_3$ $L1_2$ phase, which is the ground state of Mn-Ni system.

Accoding to the current studies, the fcc Mn-Ni binary system has two GS in terms of both formation and mixing enthalpies (Fig. 8(a)): antiferromagnetic $L1_0$ MnNi which has been observed with X-ray diffraction in Refs.[69,70] (see Fig. 7(a)) and ferromagnetic $L1_2$ $MnNi_3$ at 75at.%Ni which has been observed in (works cited in Ref.[71]) (see Fig. 7(b)). The formation enthalpy of $L1_0$ MnNi is the most negative among all studied structures, including ternary and quaternary (see Table III).

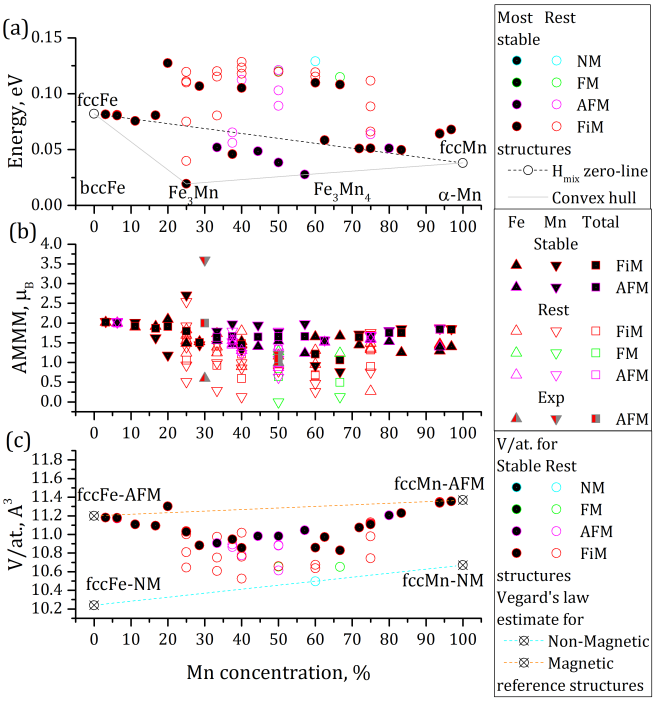

FIG. 6: (a) Enthalpy of formation, (b) average magnitudes of magnetic moments per atom, (c) volume per atom of fcc Fe-Mn structures calculated using DFT. The notation is the same as in Fig. 5. Experimental data is adapted from Ref.[68]

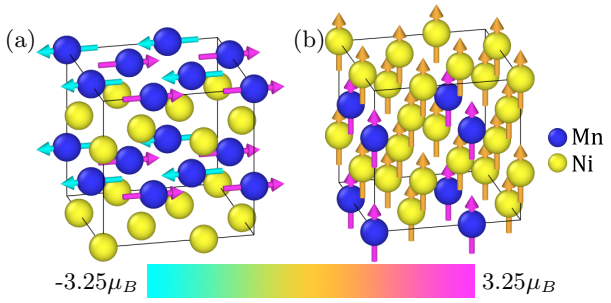

FIG. 7: Atomic structure and magnetic moments of the binary Mn-Ni ground states calculated in a conventional fcc 2x2x2 super cell using collinear magnetism in DFT: (a) MnNi and (b) $MnNi_3$. The color code of the arrows shows the magnitudes of magnetic moments.

Volumes per atom for NM structures are in a good correspondence with the Vegard's law estimate for NM structures (Fig. 8(b)), whereas the values of volumes per atom for both FM and FiM structures become highly overestimated, when moving from pure elements to the equiatomic concentration, compared to the Vegard's law estimate for magnetic structures. Values of volumes per atom for the structures with Mn concentration between 0 and 30at%, which are mostly FM, are in an excellent correspondence with the experimental data from Refs.[72,73], whereas for higher Mn concentration the agreement gradually becomes worse, compared to experimental data from Refs.[74,75].

Regions of stability of different magnetic configurations are divided by antiferromagnetic $L1_0$ MnNi. Magnetic ordering of the most stable sturctures with more than 50at.% Mn concentration is AFM or FiM (Fig. 8(c)), and at Mn concentrations lower than 25at.% the magnetic ordering of the most stable structures is FM, which is consistent with the experimental observations[76–78]. The boundary of this division is approx. 33 at.%Mn. The value of AMMM of manganese is growing with the increasing Ni concentration, being equal to the value of magnetic moment for fcc AFMSL Mn (see Table II) at concentrations close to 0at.% Ni, and to the value of magnetic moment of Type I atom in AFM α-Mn at concentrations close to 100at.% Ni (see Table II). The values of AMMM are underestimated compared to the experimental results from Ref[79] up to 20at.% Mn, but are close at higher Mn concentration. The values of AMMMs for FM structures increase with the increase of Mn concentration. The AMMM of Ni is very close to the experimental values from Ref.[79].

From current studies, Mn atoms in the $L1_0$ MnNi form two sublattices, which are antiferromagnetically ordered to each other, with the magnitude of magnetic moment per atom of 3.15 μ_B and Ni atoms do not have magnetic moment. The AMMM of 0 for Ni closely corresponds to one of the estimates in Ref.[80], and the AMMM for Mn lies between the estimates from Refs.[80], 4μ_B, and Ref.[81], 2.4μ_B. Simulation and experimental results from Ref.[82] show that both bulk and thin film $Mn_{50}Ni_{50}$ have Mn in high-spin state with values of magnetic moment per atom of 2.8-3.9μ_B and Ni with strongly reduced values of magnetic moment per atom. Total AMMM of 1.58μ_B is very close to the values from Ref.[75], 1.9μ_B and adapted from Ref.[80], 2μ_B.

In the fcc $L1_2$ $MnNi_3$ FM structure, Mn atoms have the magnetic moment of 3.252 μ_B, and Ni atoms have on average the magnetic moment of 0.53 μ_B, which closely corresponds to the experimental measurements from Ref.[78] with $\mu_{Mn} = 3.18\ \mu_B$ and $\mu_{Ni} = 0.3\ \mu_B$, Ref.[76] with $\mu_{Mn} = 3.7\ \mu_B$ and $\mu_{Ni} = 0.6\ \mu_B$, and Ref.[77] with $\mu_{Mn} = 3.6\ \mu_B$ and $\mu_{Ni} = 0.31\ \mu_B$. Total AMMM of 1.21μ_B is also very close to the experimental value of 1.1μ_B from Ref.[77].

C. Ternary Subsystems

In this subsection, the results of DFT calculations at 0 K for Fe-Cr-Mn, Fe-Mn-Ni and Cr-Mn-Ni ternary structures including the underlying binaries are presented and analysed. Since the methodology and the results for Fe-Cr-Ni ternary alloy are similar to one used in Ref.[21], they are described in the Supplementary materials, Section S I.D. ECIs have been obtained based on the chosen set of undecorated clusters (6 two-body, 2 three-body and 1 four-body) which gives for ternaries 18 two-body, 10 three-body and 5 four-body decorated clusters.

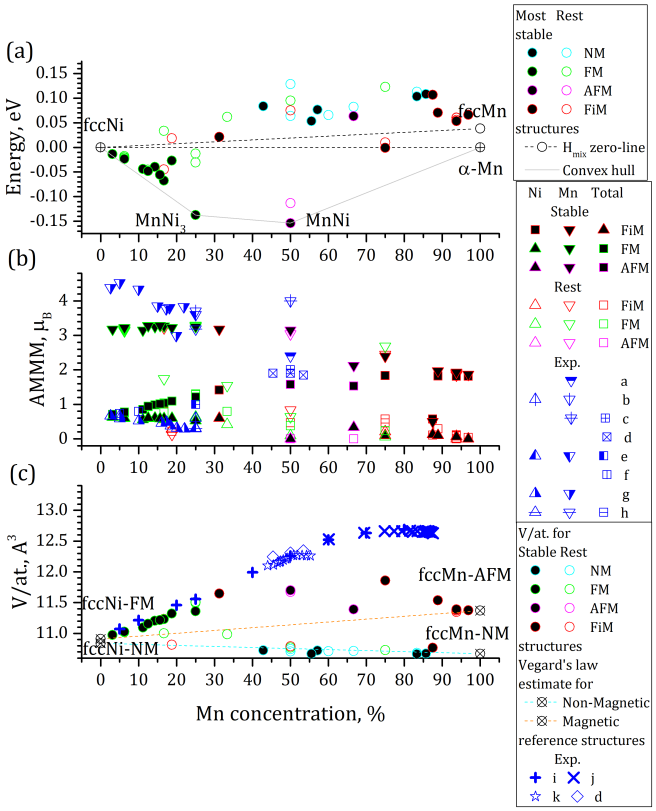

FIG. 8: (a) Enthalpy of formation, (b) average magnitudes of magnetic moments per atom, (c) volume per atom of fcc Mn-Ni structures calculated using DFT. The notation is the same as in Fig. 5. Experimental data is adapted from: [a] - Cable *et. al*[81], [b] - Petrillo *et. al*[76], [c] - Kasper *et. al*[80], [d] - Kren *et. al*[75], [e] - Paoletti *et. al*[77], [f] - Tange *et. al*[83], [g] - Kajzar *et. al*[79], [h] - Shull *et. al*[78], [i] - Gokcen[72], [j] - Honda *et. al*[73], [k] - Pearson *et. al*[74].

Enthalpies of formation, enthalpies of mixing, volumes per atom and AMMMs for all ternary alloys are presented as the color-coded ternary diagrams, where color represents values of a property of choice and three axis correspond to the concentrations of respective chemical elements. In such a representation, only one value for each composition can be presented, which is chosen to be the value of the most stable structure for each composition on all ternary plots. Values in between are interpolated to give the more readable picture.

The enthalpies of mixing from DFT calculations and CE are compared in the Supplementary materials, Fig. S 6-S 9.

1. *Fe-Cr-Mn Ternary*

The final set of structures applied for the development of CE model for fcc Fe-Cr-Mn ternary consists of 260 structures, 89 of which are three-component and the resulting CVS is 11.95 meV. The absolute values of ECIs in fcc Fe-Cr-Mn system are the smallest in comparison with other ternary systems (Fig. 9(a)). Moreover, the 1NN and 2NN interactions are the strongest ones, which shows that the interactions of further neighbors and multi-body ECIs are almost negligible in Fe-Cr-Mn alloys.

There are three ternary ground states in terms of enthalpy of mixing: $FeCr_4Mn$, which has a similar structure to Fe-*Me* from Ref.[84], Fe_5Cr_2Mn, which is a derivative of $L1_2$[84], Fe_6CrMn, which is the ABC_6-type structure, observed previously in $CuMnPt_6$[85,86] that evolved through Cu_3Au-type alloy, in $Cu[Mn,Fe]Pd_6$[87] and in Ni_6SiTi[88]. In terms of enthalpy of formation there are no ground states and the structures in general are more unstable in the Cr-rich region (Fig. 10(b)). No stable ternary Fe-Cr-Mn fcc intermetallic phases are found in literature[89]. Metallographic analysis, X-ray diffraction and electron-probe micro analysis results show that the single-phase region of the fcc phase is only extended up to 5at.% Cr and up to 38at.% Mn in the ternary phase diagram at 923 K, whereas for Mn content less than 25at.% the coexistence of fcc and fcc+σ phases is observed[90].

The Cr-rich region, limited at 70at.% Cr on Cr-Mn edge and 30at.% Cr on the Fe-Cr edge shows the non-magnetic ordering, and the rest of the alloy shows the ferrimagnetic ordering (Fig. 10(c)) - the separation lines are shown by green dashed lines, which are constrained on ends (binary edges) by the compositions of DFT calculated structures.

Volume-concentration dependency for Cr-rich NM region strongly corresponds to the Vegard's law estimate, whereas for FiM region the volume per atom increases with the AMMM of the alloy and it has the highest values in the Fe-rich region (Fig. 10(d)). The concentration dependency behavior of studied parameters resembles the interpolation of binary subsystems plots.

2. *Cr-Mn-Ni Ternary*

The cross-validation score between CE and DFT for the fcc Cr-Mn-Ni ternary system is 12.74 meV. The final database of structures consists of 250 structures, 66 of which are three-component. Absolute values of 1NN ECIs are positive and the largest among other ternaries (Fig. 9(c)).

The ternary alloy ground state in terms of enthalpy of mixing and enthalpy of formation (Fig. 11(a,b)) is $CrNi_2Mn$, previously not described in a literature, which has the same space group (*P4/mma*) and magnetic space group (*Pm'm'm*) as previously predicted Fe_2CrNi phase from Ref.[21] (see Table III), althought the relative magnitudes of magnetic moments are different: in Fe_2CrNi, the absolute value of magnetic moment of Cr (1d) is the highest, 2.436 μ_B, followed by Fe (1g and 1f) with values 2.046 μ_B and 2.123 μ_B, and Ni (1a) having the lowest AMMM of 0.153 μ_B; and in $CrMnNi_2$ the highest value of magnetic moments is held by Mn (1a), equal to 2.872 μ_B;

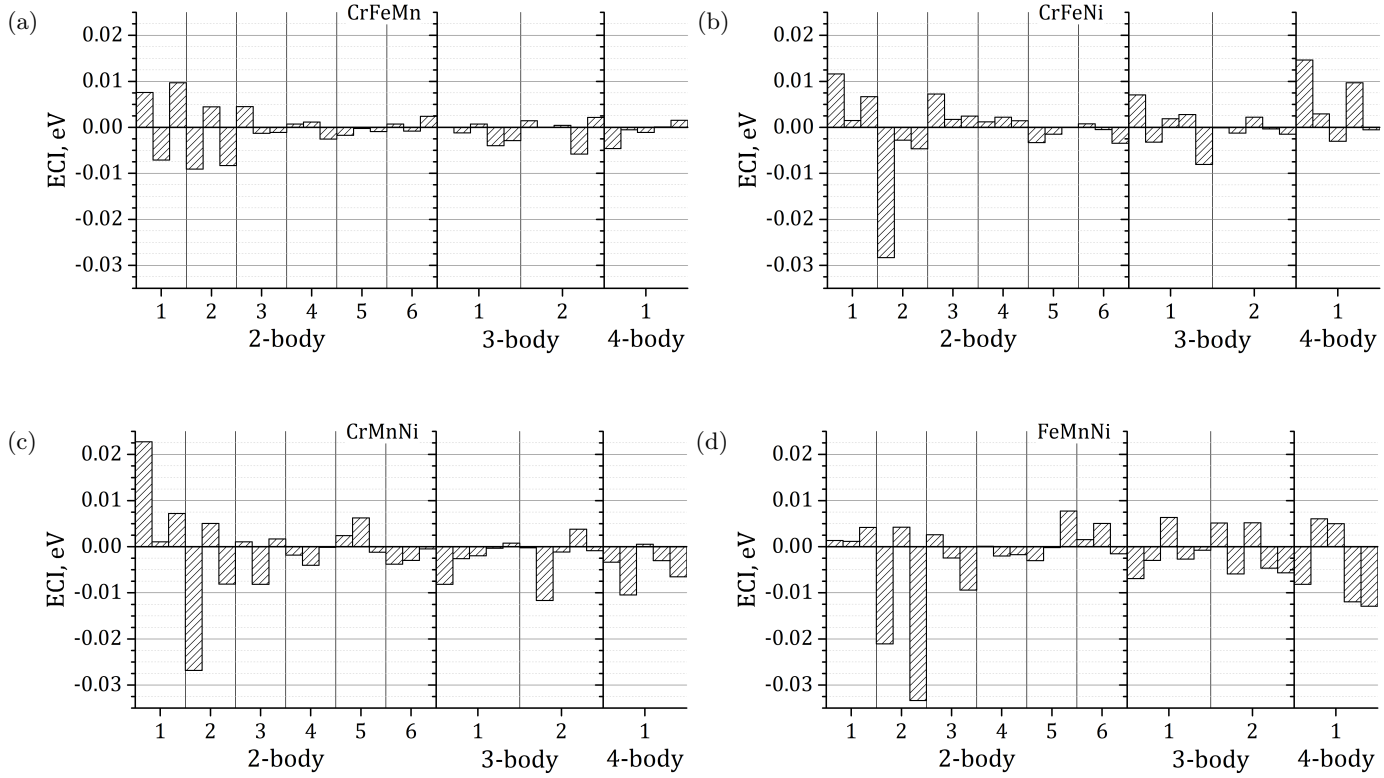

FIG. 9: ECIs for ternary subsystems.

1d is similarly occupied by Cr with AMMM of 2.543 μ_B; 1g and 1f are occupied by Ni atoms with the values of magnetic moments equal to 0.133 μ_B and 0.338 μ_B, respectively. Since ordered ternary structures with negative formation enthalpy were not found in Fe-Cr-Mn and Fe-Mn-Ni systems, the $CrNi_2Mn$ is the most stable ternary compound. Ternary ground state $CrNi_2Mn$ and the ground states of underlying binary subsystems are marked on Fig. 11 as filled circles.

The Cr-Mn-Ni system has 3 regions of magnetic ordering (Fig. 11(c)) - non-magnetic in Cr-righ region, limited at 70at.% Cr in ternary ($Cr_{70}Mn_{15}Ni_{15}$), 30at.% Cr at Cr-Mn binary and 50at.% at Cr-Ni binary; ferromagnetic in Ni-rich region, limited at 50at.% Ni in Cr-Ni binary and 30at.% Ni at Mn-Ni binary; and the rest of alloys are ordered ferrimagnetically - all indicated by green dashed lines. Values of volumes per atom in the NM region correspond to the Vegard's law estimate in the Cr-Mn region and are underestimated for Ni-rich region (Fig. 11(d)). Volume per atom in FM and FiM regions increases with the increasing average magnitude of magnetic moment per atom in the alloy. Concentration dependency behavior of studied parameters resembles the interpolation of binary subsystems plots.

3. Fe-Mn-Ni Ternary

The total number of structures used in the CE method for the fcc Fe-Mn-Ni system is 210 with 46 three-component structures and the CVS is 11.83 meV. ECIs (Fig. 9(d)) in 2NN are negative and the strongest compared to other 2-body interactions. They have also the largest absolute value compared to other ternary subsystems.

In terms of enthalpy of mixing there is one ternary ground state, fcc $FeMnNi_6$ (Fm-3m) (Fig. 12(a)). However, none of structures is a ground state in terms of formation enthalpy. Ground states of underlying binary subsystems are indicated by filled circles on all subplots of Fig. 12. In general, structures with negative enthalpy of formation are located in the Ni-rich region, due to the presence of fcc stabilizing Ni in sufficient concentrations (Fig. 12(b)).

Average magnitudes of magnetic moments per atom from current calculations are compared to the neutron diffraction data from Refs.[91,92] for alloys with composition $Fe_{75-x}Ni_xMn_{25}$, x=0-25at.%. AMMM for FM and FiM structures, obtained in current work, lay between the AMMM for antiferromagnetic structures at 77 K and paramagnetic structures.

Aging experiments for $Fe_{75}Ni_{20}Mn_5$[93] and $Fe_{7.8}Mn_{8.2}Ni_{84}$[94] have indicated the low-temperature

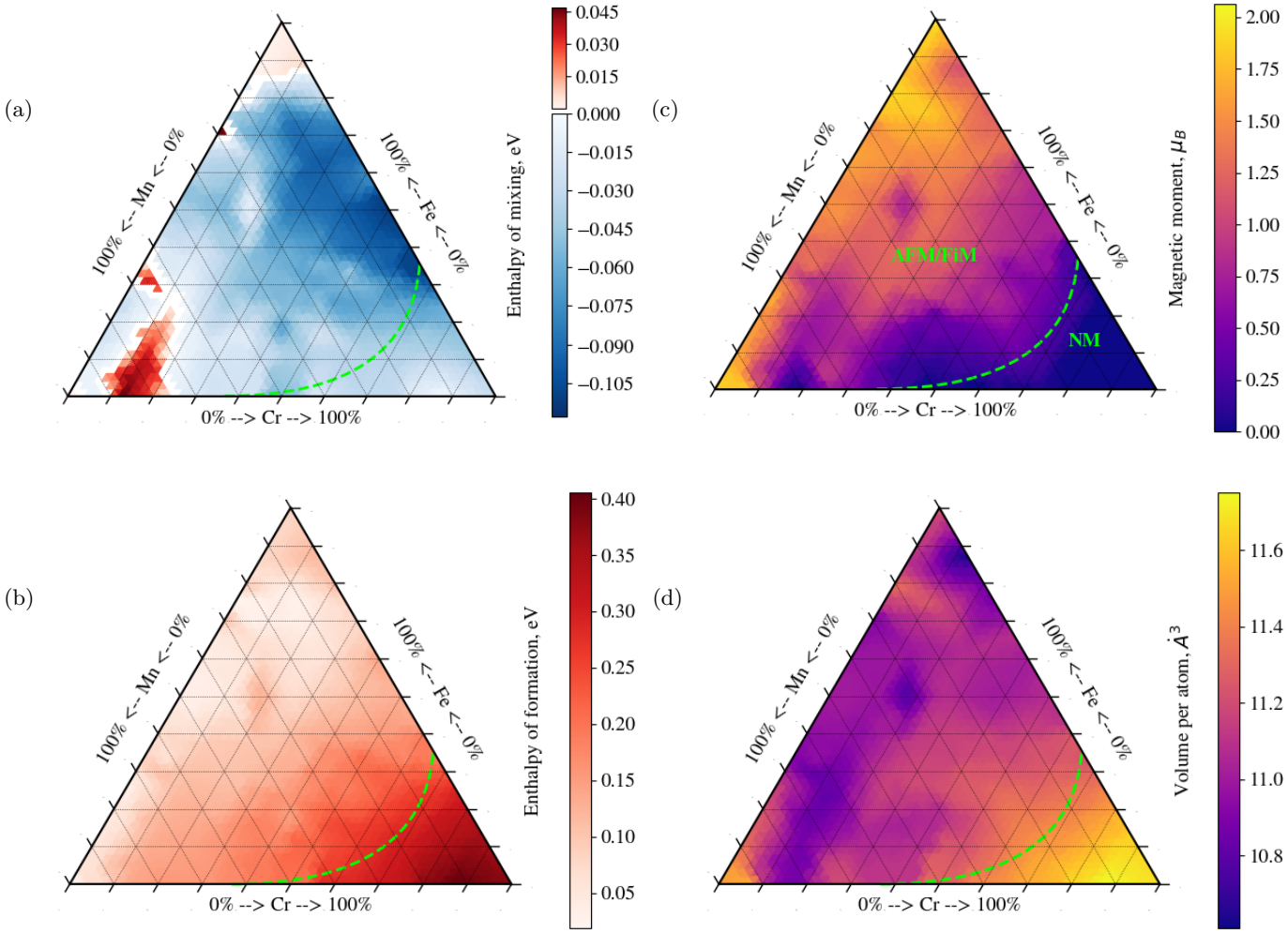

FIG. 10: Interpolated data obtained from the results calculated using DFT for the most stable structures and magnetic configurations for Fe-Cr-Mn alloys on fcc lattice: (a) enthalpy of mixing; (b) enthalpy of formation; (c) average magnitudes of magnetic moments; and (d) volume per atom. Green dashed lines separate the regions with different predominate magnetic configuration, which are indicated in (c).

precipitation of the $L1_0$ MnNi and $L1_2$ $MnNi_3$ phases.

Magnetic stability is divided into two regions (Fig. 12(c)) - ferromagnetically ordered Ni rich region, limited at 50at.% Ni in ternary ($Fe_{25}Mn_{25}Ni_{50}$) and 40at.% Ni at Fe-Ni binary, and the FiM ordered region in the rest of the alloy - all regions indicated by green dashed lines. Simulation results are in a good correspondence with the experimental magnetic phase diagram for ternary[95,96] and pseudobinary $Fe_{50}Ni_xMn_{50-x}$, x=9.88-39.74at.%[97]. The lines separating the regions of stability of FM and AFM, presented in Fig. 12(c) are in good agreement with separation line obtained experimentally at 4 K in Ref.[95] (indicated as green dotted line in Fig. 12(c)) and the experimental line of phase transition with changing Ni concentration from Ref.[97] (indicated as solid green line in Fig. 12(c)). The antiferromagnetic $L1_0$ MnNi structure has a very negative enthalpy of formation, which also corresponds to the ordered MnNi region in Ref.[98].

As Fe-Mn-Ni ternary is fully magnetic, the volume per atom has overestimated values compared to the Vegard's law estimate and tends to increase with the increasing AMMM (Fig. 12(d)). The X-ray diffraction results for induction-melted specimens with varying composition $Fe_{75-x}Ni_xMn_{25}$, x=0-25at.%, annealed for 15 hours at 900 °C and water quenched[92], indicate that all 3-component specimens have the disordered fcc lattice with the average volume per atom of 11.69 $Å^3$, which is close to the results of current calculations - 11.33 $Å^3$.

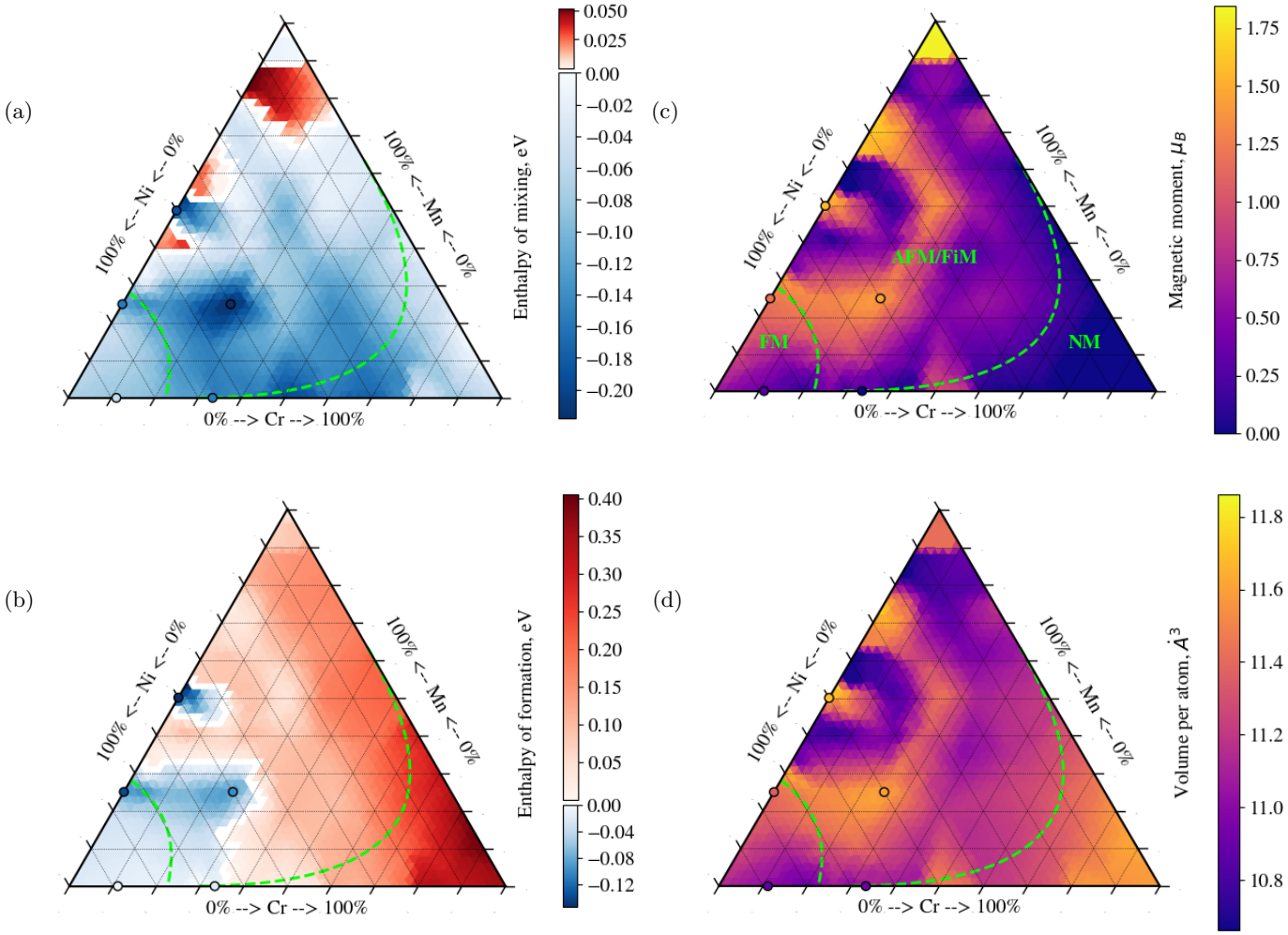

FIG. 11: Interpolated data obtained from the results calculated using DFT for the most stable structures and magnetic configurations for Cr-Mn-Ni alloys on fcc lattice: (a) enthalpy of mixing; (b) enthalpy of formation; (c) average magnitudes of magnetic moments; and (d) volume per atom. Green dashed lines separate the regions with different predominate magnetic configuration, which are indicated in (c). Filled circles represent ground states.

D. Fe-Cr-Mn-Ni Quaternary System

The final database of structures for fcc Fe-Cr-Mn-Ni system contains all other subsystems databases and consists of 831 structures total, 191 of which are four-component. The cross-validation score between CE and DFT is equal to 12.95 meV. Differences between DFT and CE enthalpies of mixing for the most stable structures of all studied compositions can be seen in Figs. 14(a) and 14(b). A chosen set of undecorated clusters gives for quaternary system 36 two-body, 28 three-body and 15 four-body decorated clusters. ECIs for quaternary systems are represented in Fig. 13 (note that the ECIs scale is different compared to ternary and binary subsystems). The exact values of ECIs for quaternary system are given in the Supplementary materials, Table S I.

Since DFT calculations in current studies give the results for 0 K and do not take into account the pressure, the concentration dependence of any chosen property can be represented analogously to how it has been done for ternary components - as a color-coded diagram depending on the concentration of 4 components. In the authors' opinion, the most representative way to illustrate the varying concentration of 4 components is the tetrahedron representation, where each vertex corresponds to the concentration of considered element. The transformation of a tetrahedral four-component coordinates into 3D cartesian coordinates have been worked out in Refs.[99,100]. In such a representation, similarly to a ternary case, only one value per composition can be represented, and therefore in following plots only values for the most stable structures for each composition are shown.

Quaternary alloy ground state in terms of both mixing

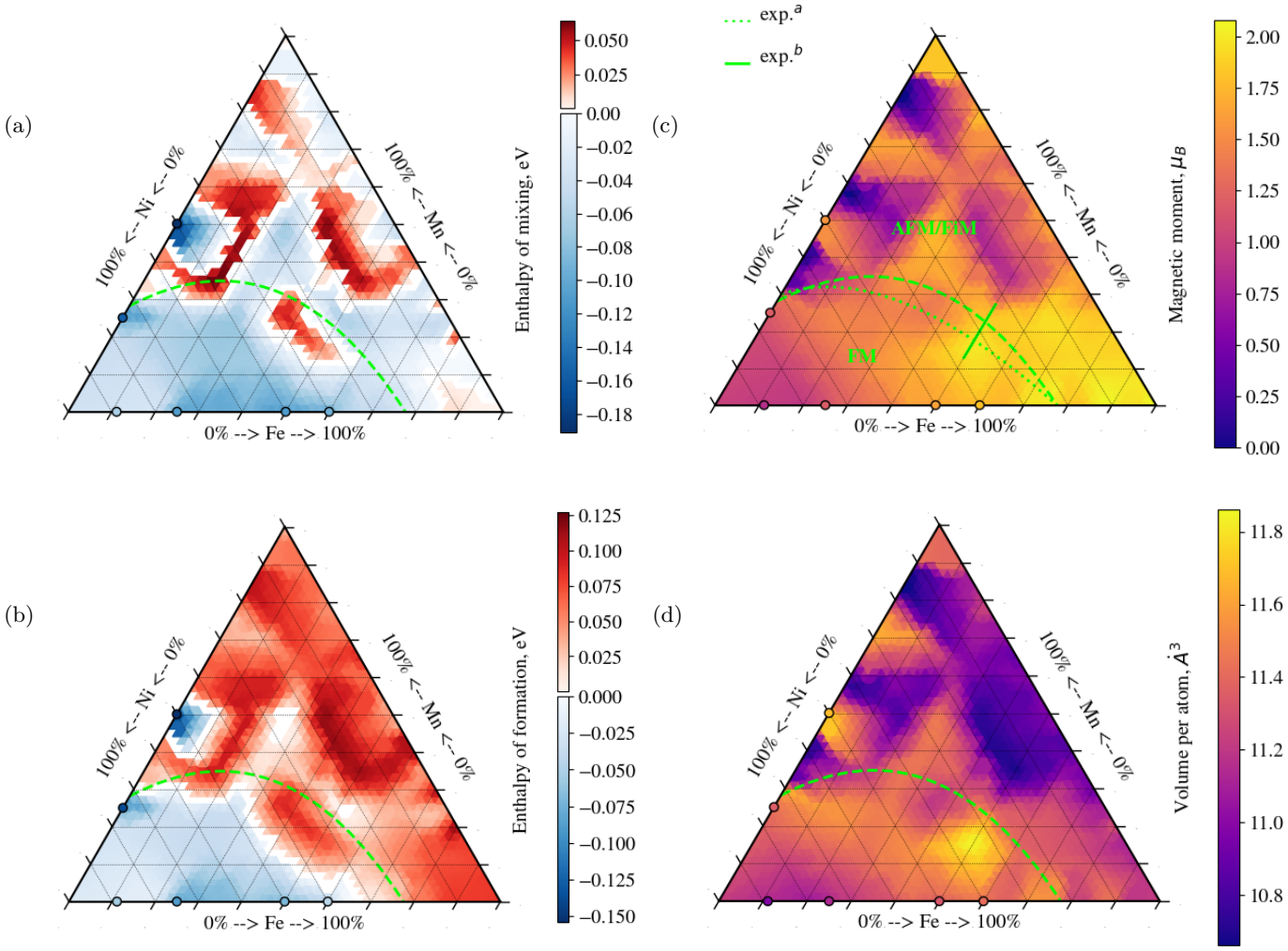

FIG. 12: Interpolated data obtained from the results calculated using DFT for the most stable structures and magnetic configurations for Fe-Mn-Ni alloys on fcc lattice: (a) enthalpy of mixing; (b) enthalpy of formation; (c) average magnitudes of magnetic moments; and (d) volume per atom. Green dashed lines separate the regions with different predominate magnetic configuration, which are indicated in (c). Filled circles represent ground states. Experimental data is adapted from [a] Ref.[95] (line that separate the regions of FM and AFM stability) and [b] Ref.[97] (line of FM-AFM magnetic phase transition with the change of Ni concentration).

and formation enthalpies (Fig. 14(a,c)) is $FeCr_2MnNi_4$ ($I4/mmm$), which is not found in literature, with the structure being the derivative of previously described ABC_6. Its atomic and magnetic configuration is illustrated in Fig. 15. Cr atoms are ordered as simple cubic structure, Fe and Mn atoms are oredered as fcc and Ni atoms show the layered structure with fcc[100] ordering within the layer.

Transmission electron microscopy of $Fe_{10}Ni_7Mn_6Cr_{77}$ (wt.%) alloy shows the pronounced precipitation within martensite and degenerate precipitation within the retained austenite[101]. Single-phase fcc near-equiatomic $[FeNiMn]_{82}Cr_{18}$ alloy was obtained with the arc-melting and homogenization, and remained stable under deformation[12]. Antiferromagnetic austenitic state is observed for $Fe_{61.5}Mn_{23}Ni_7Cr_{8.5}$ alloy[102].

Region of fcc stability from the points of view of the negative formation enthalpy is close to the estimate of higher limit of fcc stability from the point of view of VEC (8 valence electrons per atom). It is localized near the Ni corner and for the quaternary and most underlying subsystems the Ni concentration should be minimally 25at.%, with the exception of the following: 40at.%Ni for Fe-Ni binary; 50at.%Ni for Cr-Mn-Ni ternary; and 67at.%Ni for Cr-Ni binary.

Quaternary alloys in the middle of the phase diagram, where the concentration of every constituting element is larger than 12.5at.%, show ferrimagnetic ordering, and the alloys near the faces of the phase diagram show the ordering of neighboring lower-compound structures; with

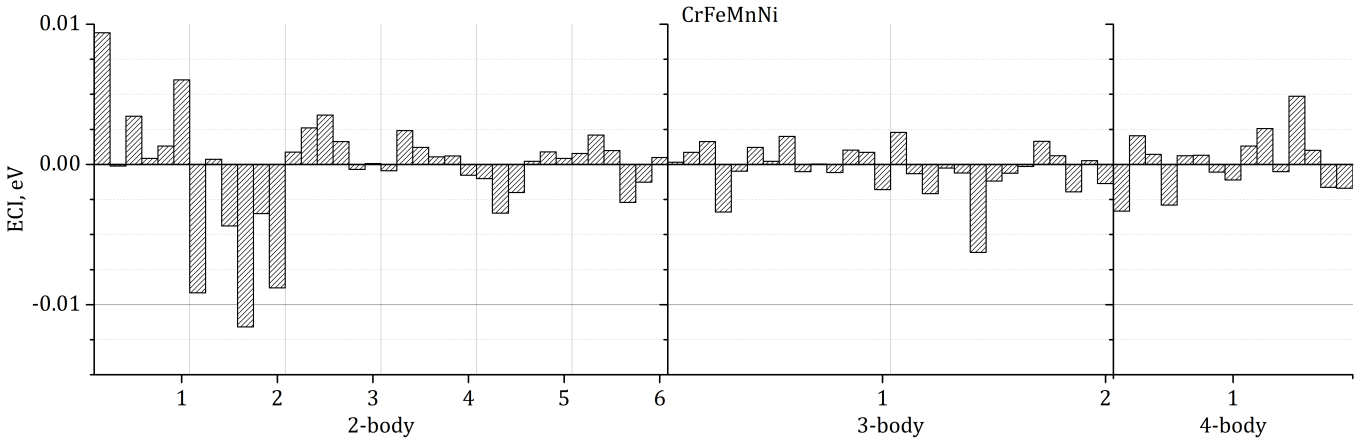

FIG. 13: ECIs for quaternary system.

small NM region in Cr-rich part, limited at 62.5at.% Cr in the quaternary ($Cr_{62.5}[FeMnNi]_{37.5}$) (Fig. 14(d)). The magnetic ordering of the most stable structures at each concentration were analysed. Resulting 264 data points in the whole concentration range were interpolated to produce the theoretical magnetic phase diagram of the fcc Fe-Cr-Mn-Ni system, which is presented in Fig. 16. It should be noted that all the studied structures are ordered atomic structures with relatively high symmetry. Values of volumes per atom (Fig. 14(e)) have the positive correlation with the values of the average magnitudes of magnetic moments per atom for the FiM region, observed in the major part of the quaternary system. AMMM and volume per atom from all studied binary, ternary and quaternary structures with VEC larger than the critical value of 6.97 from Refs.[22,23] have been collected to illustrate the magneto-volume relation. It is represented in Fig. 17 and it is clearly seen that the volume per atom is increasing with the increase of the average magnitude of magnetic moments for all subsystems and quaternary system. However, for Fe-Cr-Ni ternary subsystem, the rate of this change is the biggest. It means that AMMM are strongly affected by the change of volume, compared to other subsystems. This fact may be responsible for the high swelling effect of Fe-Cr-Ni alloys. Also, the AMMM is increasing with the increase of volume slower in Fe-Cr-Mn-Ni quaternary than in Fe-Cr-Ni ternary, which supports the results of reduced swelling in Fe-Cr-Mn-Ni HEA compared to Fe-Cr-Ni in Ref.[8].

The enthalpy of formation, volume per atom, average magnitudes of magnetic moments, type of magnetic ordering, as well as crystalographic symmetry and magnetic symmetry for the most stable intermetallic structures of Fe-Cr-Mn-Ni alloys are given in Table III.

IV. FINITE TEMPERATURE PHASE STABILITY OF FE-CR-MN-NI ALLOYS

Finite-temperature phase stability of Fe-Cr-Mn-Ni alloys was analysed with the semi-canonical Monte Carlo simulations using ECIs obtained from the combination of CE and DFT calculations. MC simulations were performed for the 264 different compositions in the whole concentration range in the 10at.% concentration mesh.

As a result of MC simulations, the mixing enthalpies and the many-body probability functions has been obtained. The last have been subsequently used in order to calculate the configurational entropy and the Warren-Cowley SRO parameters.

Order-Disorder Transition (ODT) temperature (T_{ODT}) in the current work was identified as the temperature above which the system is disordered and below - shows partial ordering. The chemical ordering strongly affects both the entalpy of mixing and the configurational entropy of mixing of the studied system. Therefore, the thermodynamic potential which includes both these values, such as free energy of mixing, would accurately represent the order-disorder transition. Hence, T_{ODT} in this work was identified via the inflection point on the free energy of mixing versus the temperature curve, which refers to the change of sign of second derivative of the free energy of mixing as a function of temperature.

Since MC simulations used in this work are based on the lattice gas model, they do not take into account neither the change of the state of matter nor the change of lattice. Therefore, all phase transitions are treated as ordering-related transitions, and the transition at highest temperature for a chosen composition is interpreted as the order-disorder transition.

TABLE III: Chemical composition, lattice symmetry with Wyckoff position, magnetic symmetry with Wyckoff position, magnetic moment on each magnetic Wyckoff position (in μ_B), AMMM from present work and found in experimental literature (in μ_B), magnetic ordering, volume per atom from present work and found in experimental literature (in Å^3), and the formation enthalpy of the most stable intermetallic phases with negative H_{form} (in eV) in fcc quaternary Fe-Cr-Mn-Ni system.

Composition	Symmetry, Wyckoff	Mag. symm., Wyckoff	$MM_{W.p.}$, $[\mu_B]$	AMMM, $[\mu_B]$ Current	AMMM, $[\mu_B]$ Exp.	Magnetic ordering	Vol./at., [Å^3] Current	Vol./at., [Å^3] Exp.	H_{form}
$CrNi_2$	*Immm*	-		0		NM	10.92	11.36[a]	-0.018
	Cr_1 2 a	Cr_1 2 a	0						
	Ni_1 4 e	Ni_1 4 e	0						
$CrNi_8$	*I4/mmm*	*C2'/m'*		0.28	0.16[b]	FiM	10.89		-0.007
	Cr_1 2 a	Cr_1 2 a	-0.687						
	Ni_1 8 h	Ni_1 4 g	0.199						
	Ni_2 8 i	Ni_2 8 j	0.278						
		Ni_3 4 i	0.178						
Fe_3Ni_2	*I4/mmm*	*C2'/m'*		1.81		FM	11.42	11.56[c]	-0.043
	Fe_1 4 e	Fe_1 4 i	2.591						
	Fe_2 2 b	Fe_2 2 d	2.652						
	Ni_1 4 e	Ni_1 4 i	0.607						
FeNi	*P4/mmm*	*Cmm'm'*		1.65	1.64[shull] 1.52[d]	FM	11.33	11.53[e]	-0.069
	Fe_1 1 d	Fe_1 2 c	2.661						
	Ni_1 1 a	Ni_1 2 a	0.631						
$FeNi_3$	*Pm-3m*	*Pm'm'm*		1.2	1.21[shull] 1.12[d]	FM	11.14	11.21[e,a] 11.23[f]	-0.092
	Fe_1 1 a	Fe_1 1 a	2.914						
	Ni_1 3 c	Ni_1 1 f	0.631						
		Ni_2 1 d	0.588						
		Ni_3 1 g	0.673						
$FeNi_8$	*I4/mmm*	*P-1*		0.86	0.85[d]	FM	10.99	10.98[c]	-0.053
	Fe_1 2 a	Fe_1 1 a	2.814						
	Ni_1 8 i	Ni_1 2 i	0.643						
	Ni_2 8 h	Ni_2 2 i	0.599						
		Ni_3 2 i	0.604						
		Ni_4 2 i	0.604						
MnNi	*P4/mmm*	*P_Bmna*		1.58	1.9[j] 2.0[g]	AFM	11.7	12.27[h,i] 12.31[j]	-0.154
	Mn_1 1 d	Mn_1 2 d	3.151						
	Ni_1 1 a	Ni_1 2 b	0						
$MnNi_3$	*Pm-3m*	*Pm'm'm*		1.21	1.1[k]	FM	11.36	11.56[f,a]	-0.137
	Mn_1 1 a	Mn_1 1 a	3.252						
	Ni_1 3 c	Ni_1 1 f	0.5						
		Ni_2 1 d	0.555						
		Ni_3 1 g	0.537						
$CrFe_2Ni$	*P4/mmm*	*Pm'm'm*		1.69		FiM	11.37		-0.026
	Cr_1 1 c	Cr_1 1 d	-2.436						
	Fe_1 2 e	Fe_1 1 g	2.046						
	Ni_1 1 a	Fe_2 1 f	2.123						
		Ni_1 1 a	0.153						
$CrMnNi_2$	*P4/mmm*	*Pm'm'm*		1.47		FiM	11.6		-0.098
	Cr_1 1 c	Cr_1 1 d	-2.543						
	Mn_1 1 a	Mn_1 1 a	2.872						
	Ni_1 2 e	Ni_1 1 g	0.133						
		Ni_2 1 f	0.338						
$Cr_2FeMnNi_4$	*I4/mmm*	*P-1*		1.36		FiM	11.49		-0.068
	Cr_1 4 c	Cr_1 1 g	-2.529						
	Fe_1 2 a	Cr_2 1 f	-2.539						
	Mn_1 2 b	Fe_1 1 b	2.432						
	Ni_1 8 f	Mn_1 1 h	2.856						
		Ni_1 1 a	0.147						
		Ni_2 1 d	0.109						
		Ni_3 1 e	0.146						
		Ni_4 1 c	0.113						

[a] - Jung[103], [b] - Takano *et. al*[104], [c] - Owen *et. al*[105], [d] - Reck *et. al*[106], [e] - Wakelin *et. al*[107], [f] - Bhatia *et. al*[108], [g] - Kasper *et. al*[80], [h] - Pearson*et. al*[74], [i] - Gokcen[72], [j] - Kren *et. al*[75], [k] - Paoletti *et. al*[77]

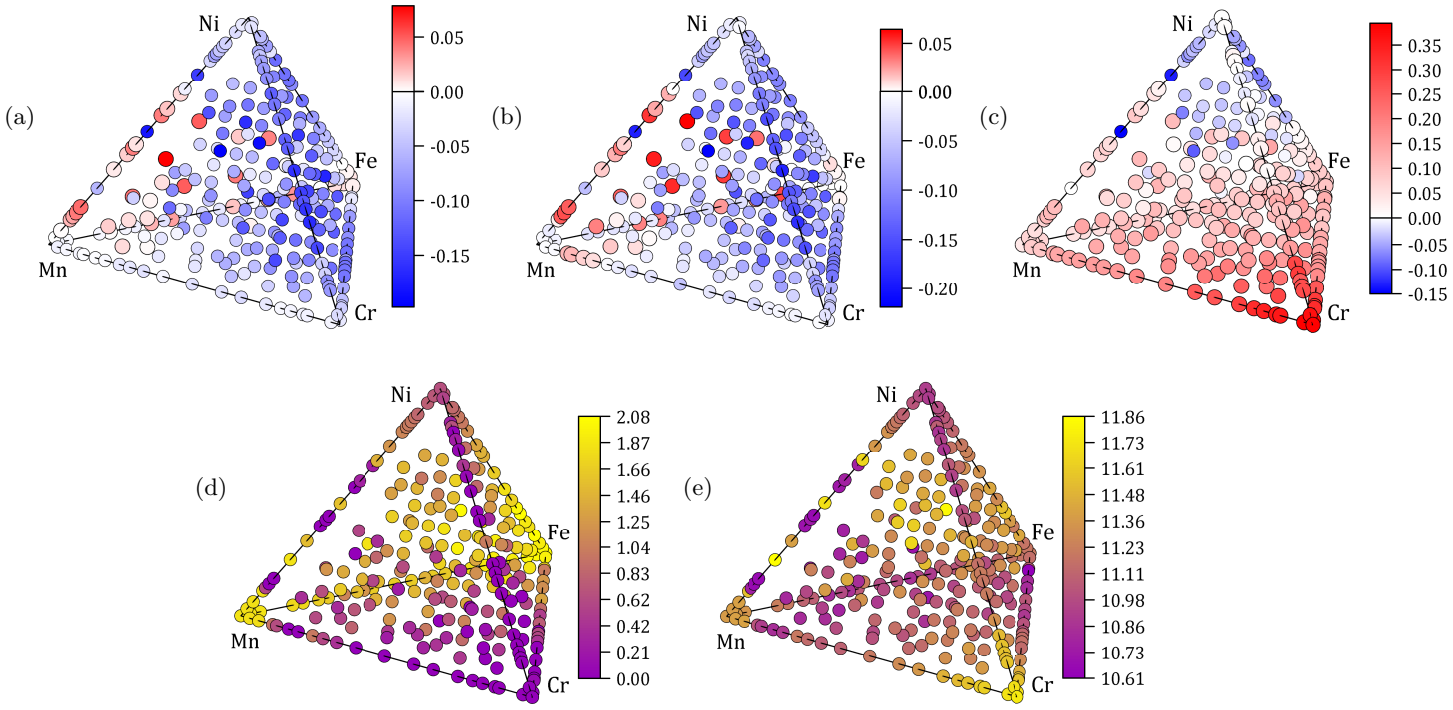

FIG. 14: The most stable structures for each considered composition calculated using DFT for Fe-Cr-Mn-Ni quaternary alloys, ternary and binary suballoys on fcc lattice: (a) enthalpy of mixing from CE; (b) enthalpy of mixing from DFT; (c) enthalpy of formation from DFT; (d) average magnitudes of magnetic moments; and, (e) volume per atom.

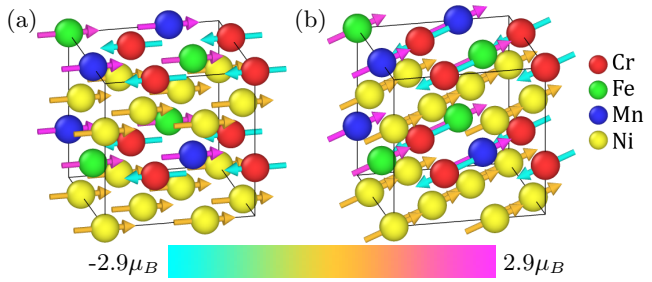

FIG. 15: Atomic structure of the predicted quaternary alloy ground state $FeCr_2MnNi_4$ in a conventional fcc unit cell using collinear (a) and non-collinear (b) magnetism in DFT.

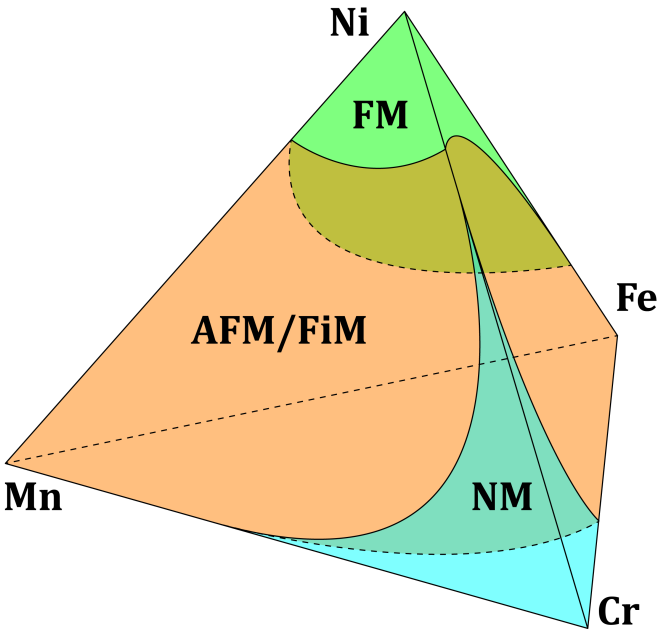

FIG. 16: Theoretical magnetic phase diagram of quaternary fcc Fe-Cr-Mn-Ni alloy based on the results of DFT calculations.

A. Configurational Entropy Calculation from a Combined Monte Carlo and Cluster Expansion

Combining Monte Carlo simulations with the cluster expansion method is the common approach for calculating thermodynamic properties once the ECIs, $J^{(s)}_{\omega,n}$, are known. Within the Monte Carlo technique, the free energies and mixing enthalpies are calculated for atomic configurations in the supercells at specific temperature ranges and chemical potentials using known energies from cluster expansion associated to clusters, and the other thermodynamic properties are calculated from these quantities (as discussed later). On the other hand, the Cluster Variation Method (CVM) is a variational method where quantities such as entropy are formulated in terms of correlation functions, which are calculated from the function minimization. The practical limitations for the Monte Carlo technique are time consuming simulations required for the thermodynamic integration method, whereas for the CVM method, which uses analytical formulas, the limitation is the need to consider the clusters with many points.

In Refs.[109,110], analytic expressions for configurational entropy in terms of Monte Carlo cluster correlation functions were applied to obtain the free energies as functions of temperature. In this work, the configurational entropy is calculated for each cluster term along the underlying subclusters included in the CE Hamiltonian. Each configurational entropy expression depends on the cluster correlation functions obtained from semi-canonical Monte Carlo simulations based on the CE ECIs[26].

In the theory developed by Kikuchi[111] the configurational entropy is expressed analytically in terms of decorated multi-body cluster correlations functions associated to a basic cluster. A basic cluster contains several subclusters - at least the 1-body subcluster and the cluster itself. For the cluster expansion of the Fe-Cr-Mn-Ni system the cluster expansion in the current work includes 10 basic clusters: four 1-body cluster, six 2-body clusters, two 3-body clusters, and one 4-body cluster, with some of the basic clusters appearing also as subclusters of other clusters, i.e. the nearest neighbor 2-body cluster in the 4-body cluster. Applying the theory of Kikuchi to the Fe-Cr-Mn-Ni with 10 basic clusters, it is possible to obtain analytic configurational entropies in terms of correlation functions, resulting in one expression per basic cluster. The cluster correlation functions are calculated from semi-canonical Monte Carlo simulations in the ATAT software[24].

The analytic expressions for configurational entropy corresponding to specific basic cluster depend on the decorated cluster probabilities, as expressed by the weight factors. Each sum of decorated probabilities in a subcluster has a weight associated to it. The values of the coefficients weighting the multi-body cluster probabilities in the configurational entropy expression include the point cluster, 6 different types of two-body, 2 three-body clusters and 1 four-body cluster. Their values are indicated in the Supplementary materials, Table S III. For example, the expression for the configurational entropy in the 4-body cluster contains the probabilities of 1-body cluster (i=1, $\omega = 1, n = 1$), the probabilities for the 1st pair cluster (i=2, $\omega = 2, n = 1$), the 1st 3-body cluster (i=8, $\omega = 3, n = 1$) and the four-body probabilities corresponding to the tetrahedron itself (i=10, $\omega = 4, n = 1$). However, during the calculation of the weights w_i for each of these subclusters it is found, in agreement with Kikuchi work[111], that the corresponding weights are $w_i = -5, 6, 0$ and -2, resulting in the expression for this basic cluster:

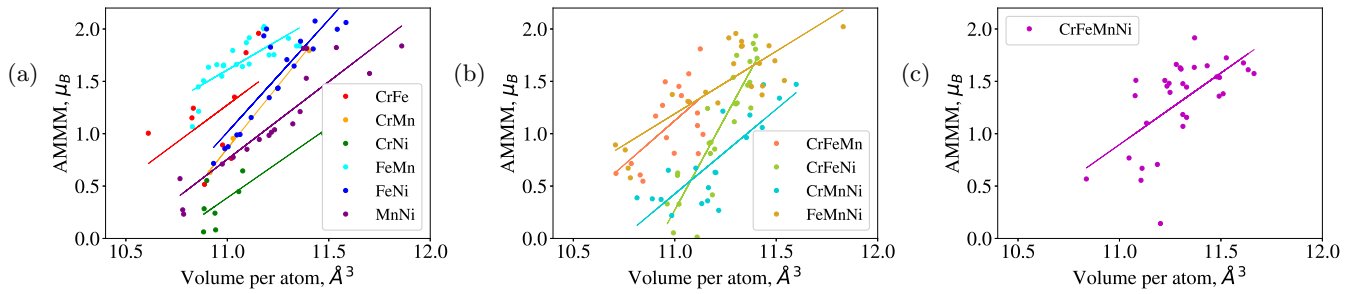

FIG. 17: Magneto-volume relation for a) binary; b) ternary and c) quaternary alloys based on DFT calculations for structures with VEC > 6.97. Filled circles represent the most stable structures for each composition; open circles indicate the rest of the structures; solid lines represent the line fitting for the most stable structures.

$$\begin{aligned} S^{conf}_{4,1}(\vec{\sigma}) = \; & -5\sum_s y^{(s)}_{1,1}(\vec{\sigma})\ln(y^{(s)}_{1,1}(\vec{\sigma})) \\ & +6\sum_s y^{(s)}_{2,1}(\vec{\sigma})\ln(y^{(s)}_{2,1}(\vec{\sigma})) \\ & -2\sum_s y^{(s)}_{4,1}(\vec{\sigma})\ln(y^{(s)}_{4,1}(\vec{\sigma})) \end{aligned} \tag{19}$$

where $\vec{\sigma}$ dependence on the $y^{(s)}_{\omega,n}(\vec{\sigma})$ is introduced to indicate that the equilibrium configuration of the Monte Carlo supercell, $\vec{\sigma}$, is associated to the temperature, T. So that the configuration $\vec{\sigma}$ is dependent on each temperature value, T. In Eq. 19 the expression for configuration entropy in the tetrahedron approximation with the weights, w_i, is indicated. For the rest of the clusters (pairs, and triplets), the weights required for the expression of configuration entropy are reported in the Supplementary materials, Table S III.

In particular, for pair clusters (nth shell denoted by $\omega = 2, n$), the entropy weights are determined by the number atomic of neighbors, Z_n, at the nth shell in the lattice of the alloy system[26] (see pp.7–8). Therefore, the entropy expression for the maximal cluster $\omega = 2, 1$ (for which $Z_1 = 12$) results in Eq. 20. This entropy formula is used further in the paper, including Figs. 18 and 19.

$$\begin{aligned} S^{conf}_{2,1}(\vec{\sigma}) = & 11\sum_s y^{(s)}_{1,1}(\vec{\sigma})\ln(y^{(s)}_{1,1}(\vec{\sigma})) \\ & -6\sum_s y^{(s)}_{2,n}(\vec{\sigma})\ln(y^{(s)}_{2,1}(\vec{\sigma})) \end{aligned} \tag{20}$$

Within the thermodynamic integration method, the configurational entropy is calculated as:

$$S^{conf}(T) = \int_0^T \frac{C_{conf}(T')}{T'}dT', \tag{21}$$

where the configurational contribution to the specific heat C_{conf} is related to the fluctuations of the enthalpy of mixing, calculated within Monte Carlo at a given temperature[112,113] as:

$$C^{conf}(T) = \frac{\langle H^2_{mix}(T)\rangle - \langle H_{mix}(T)\rangle^2}{T^2}, \tag{22}$$

where $\langle H^2_{mix}(T)\rangle$ and $\langle H_{mix}(T)\rangle^2$ are the mean and mean square average enthalpies of mixing, respectively. However, in order to perform the accurate integration of region around the transition temperature, which looks like a peak on the function of $C^{conf}(T)$, the simulations should be performed with small temperature steps, which increases the simulation time significantly.

In order to compare the results of the two methods of entropy calculations, Monte Carlo run with the thermodynamic integration routine has been performed for the equiatomic composition in a supercell of 8000 atoms starting from 3000 K down to 0 K considering 1000 equilibration steps and 2000 accumulation Monte Carlo steps per site at each temperature in steps of $\Delta T = 5$ K.

The configurational entropy corresponding to each of the 10 basic cluster obtained by the cluster expansion method, as well as the configurational entropy obtained from the Monte Carlo thermodynamically integrated method is presented and discussed in the paper of Fernández-Caballero *et al.*[26]. The configurational entropy obtained from the analytic formulation at temperatures in the range 0-1000 K is found to be sensitive to the ECIs and the Monte Carlo calculation temperature step, resulting in nonphysical values of negative entropies for certain clusters.

In the high temperature limit, the expression of configurational entropy corresponding to each of the basic clusters and the one obtained from the TDI are found to converge towards the perfect random solid solution (also known as the temperature independent Bragg-Williams approximation) for the average system composition, c_p, given by $S^{conf}_{random}(T) = -k_B\sum_p c_p\ln(c_p)$, which, in the case of equiatomic composition is equal to 1.386 k_B.

B. Free Energy of Mixing

Knowing the enthalpy of mixing and the configurational entropy, the free energy of mixing can be evaluated as $F_{mix} = H_{mix} - TS^{conf}_{mix}$, where S^{conf}_{mix} is defined as $S^{conf}_{random} - S^{conf}$. Example calculation for equiatomic

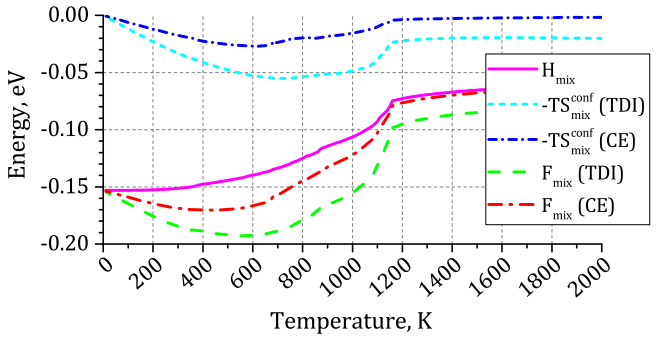

FIG. 18: Enthalpy of mixing and free energy of mixing from Monte-Carlo simulations, as well as -TS$_{conf}$ and free energies of mixing calculated using thermodynamic integration and Cluster Expansion methods for the equiatomic Fe-Cr-Mn-Ni alloy.

composition is illustrated in Fig. 18, where the free energies of mixing obtained from the basic cluster approximation corresponding to the 1st nearest neighbor 2-body cluster ($\omega = 2, n = 1$) and TDI calculations are presented.

It can be seen for the $-TS^{conf}_{mix}$ obtained from both CE and TDI methods (Fig. 18), that its contribution to the free energy of mixing is very small in the high temperature limit, which is related to the convergence towards the perfect random solid solution discussed above. On the other hand, for the temperatures below T_{ODT}, the contribution of $-TS^{conf}_{mix}$ becomes prominent and decreases the values of F_{mix} notably.

In order to demonstrate the contribution of $-TS^{conf}_{mix}$ to the F_{mix} values in the whole range of compositions of Fe-Cr-Mn-Ni alloys, there are shown in Fig. 19 the tetrahedron representations of H_{mix}, $-TS^{conf}_{mix}$ and F_{mix} at 300 K, 1000 K and 2000 K. It should be noted, that for few compositions at 300 K the values of entropy obtained from CE were negative, and hence they are not represented on the corresponding subfigures of Fig. 19.

The values of $-TS^{conf}_{mix}$ at 2000 K are substantial mainly for the compositions with the high concentration of MnNi (Fig. 19(c)). At 1000 K, which is below T_{ODT} for the major part of the compositions in the middle of the phase diagram, the values of $-TS^{conf}_{mix}$ are substantial for these compositions (Fig. 19(b)). At 300 K, where the ODT has occurred for almost all compositions, the values of S^{conf}_{mix} are non-zero (Fig. 19(a)). However, since the temperature is comparatively small the $-TS^{conf}_{mix}$ is also smaller than at 1000 K.

Since H_{mix} has been obtained from the MC simulations, it shows a clear temperature dependence. At low temperature (Fig. 19(d)), the majority of the compositions have negative H_{mix} with its values being strongly negative. When the temperature is increased (Fig. 19(e,f)), the values of H_{mix} gradually become less negative, and for some compositions the H_{mix} becomes positive.

Due to the effect of both contributions, F_{mix} has different dependence on temperature in different regions. For the compositions which are close to the vertices of the phase diagram, the trend in temperature dependence is similar to the trend in H_{mix}. On the other hand, the values of F_{mix} in the middle of the phase diagram are most negative at 1000 K (Fig. 19(h)), being even more negative than at 300 K (Fig. 19(g)), whereas at 2000 K F_{mix} is strongly negative only for structures close in composition to MnNi (Fig. 19(i)). It should be noted that the effect of some structures being more stable at elevated temperatures than at lower temperatures can be caused by the constraints of the current work, where only the fcc lattice is considered, and the vibrational and magnetic contributions are not taken into account.

C. Order-Disorder Transition Temperatures

Order-Disorder Transition temperature has been calculated for each MC simulated structure in the whole concentration range as the inflection point on the free energy of mixing versus the temperature curve for the given structure.

The effect of each element concentration on T_{ODT} has been studied on the pseudobinary compositions of type $A_x[BCD]_{(1-x)}$. The order-disorder transition temperatures as functions of concentration in pseudobinaries are shown in Fig. 20. T_{ODT} dependency on concentration for manganese has a minimum at 30at.% Mn, which is 1100 K. T_{ODT} dependency on concentration for iron has a minimum range of 22.5at.%-40at.% Fe with T_{ODT} in this range being equal to 1100 K. T_{ODT} as a function of Chromium concentration decreases with increasing Cr concentration similar to Fe up to 30at.% Cr and then continues to decrease. One of possible explanations of such behavior is that Cr at large concentrations suppresses the magnetic moments of other elements, decreasing the influence of magnetic interactions on the ordering. Also, there are no ground states with negative formation enthalpy and Cr content more than 33.3 at.%, which would require more time for atoms to reallocate themselves to the positions of preferable precipitates. Nickel pseudobinary is the most interesting because Ni is fcc-stabilizer and T_{ODT} as a function of its concentration, as opposed to other elements, increases monotonically with increasing Ni concentration. Hence, the smallest T_{ODT} equal to 400 K is observed for equiatomic fcc FeCrMn alloy without Ni, and most likely ordered as non-fcc.

The order-disorder transition temperature as a function of concentration of each element in Fe-Cr-Mn-Ni alloy for the structures from a concentration mesh and pseudobinaries is presented in Fig. 21(a). It can be seen from this plot, that the lowest temperatures of order-disorder transitions are observed in the structures with the lowest Ni concentration, exactly what is observed in the pseudobinaries. It should be noted that Ni is the fcc

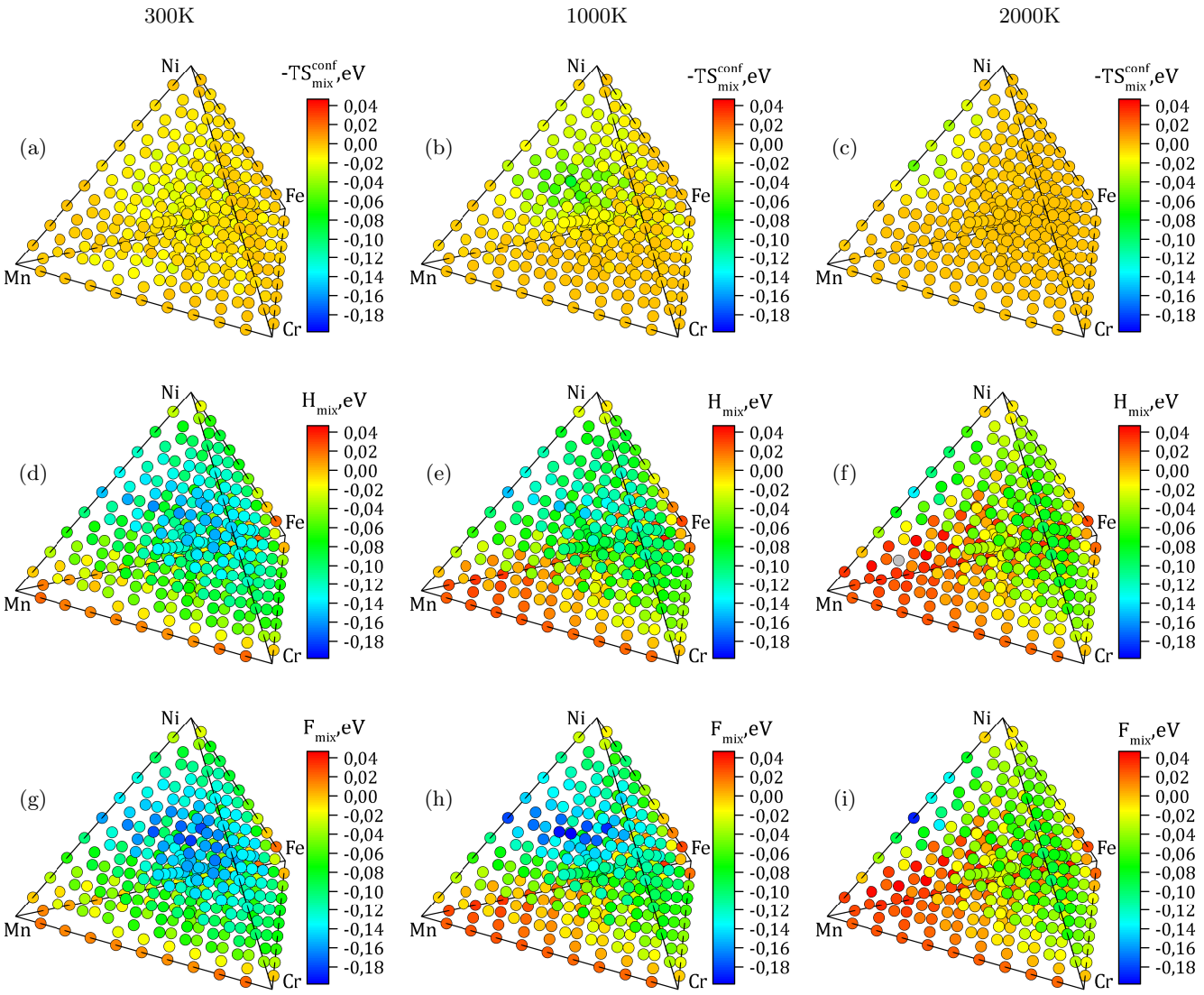

FIG. 19: Contribution of the (a-c) $-TS^{conf}_{mix}$ and the (d-f) H_{mix} to the (g-i) F_{mix} in the whole concentration range at 300 K, 1000 K and 2000 K. S^{conf} is taken from the cluster $\omega = 2, n = 1$.

stabilizer and alloys with small Ni concentration, which in this system corresponds to small VEC, may transform into non-fcc phase. Therefore the Ni content should be balanced accurately to achieve the disordered fcc single-phase composition.

In current calculations, the ORNL alloy with composition $Cr_{18}Fe_{27}Mn_{27}Ni_{28}$[8] during the cooling is disordered above 1290 K. Below that temperature, the $L1_0$ MnNi phase starts to form (see reperesentative structures in Fig. 22(c)).

The value of T_{ODT}=1290 K is lower than the temperature of the samples homogenization of 1473 K from Ref.[8], but it is higher than the temperature of recrystalization of 1173 K from the same studies, after which authors of Ref.[8] report the single phase fcc structure. This may be related to the fact that the current simulations do not take into account the effect of lattice vibrations on the evolution of the structure, which, if accounted for, should contribute to the lowering of the T_{ODT}.

It should be noted that the authors of experimental Ref.[8] state that according to the exploratory studies, equiatomic alloy does not form fcc single-phase structure, and the composition which does form it is $Cr_{18}Fe_{27}Mn_{27}Ni_{28}$ (ORNL) - the alloy with near-equiatomic composition and depleted Cr concentration. This result is supported by the estimation of VEC, where less valence electrons per atom corresponds to the lower stability of the fcc lattice, and the value for equiatomic composition (7.75) is lower than for ORNL composition (7.93). In the current work, the formation enthalpy of the ORNL composition is more negative than that of equiatomic alloy in the whole studied temperature range (see Fig. 22(c)&(e)). Moreover, the free energy of mixing at 1173 K is equal to -0.044 eV for equiatomic alloy and

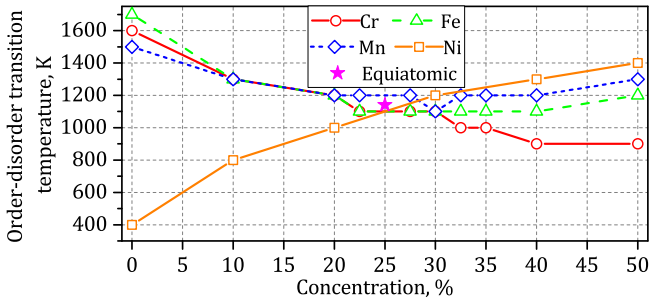

FIG. 20: Order-disorder transition temperatures as a function of each element concentration. Each data point represents different pseudobianry alloy, in which the concentration of a chosen element is equal to that on x-axis and the relative concentration of other elements is equiatomic.

-0.150 eV for ORNL alloy.

Moreover, current MC simulations show that for lower temperatures, which are still located in the range of working temperatures for fusion reactors[114], the phase composition of the alloy is divided into distinct regions: one is the $L1_0$ MnNi precipitate and the other is a combination of the quaternary and Mn-/Ni-poor ternary phases. The precipitation of the $L1_0$ MnNi phase is in line with the Cantor alloy studies from Ref.[16], where it was one of the three major precipitates that formed after annealing for 500 days at 773 K.

$L1_0$-MnNi is the most stable structure, has very strong short-range ordering (as discussed later) and Mn-Mn-Ni-Ni has been shown to have the highest cluster correlation function in Ref.[26]. Based on these facts, the analysis was made to find out the compositions, where it precipitates in Fe-Cr-Mn-Ni quaternary system. Positions and types of atoms were taken from the MC simulations at temperature 100 K. The first nearest neighbors of each atom were analysed and if at least one unit cell had the structure of $L1_0$ (2 Mn atoms and 2 Ni atoms), the atom was indicated as belonging to the $L1_0$. Indication via the unit cell makes the analysis very computationally efficient and does not yield false positive error, meaning that it does not indicate 1-layer Mn-Ni precipitations or Mn-Ni clusters which are part of more complex intermetallic compounds as Mn-Ni $L1_0$ phase. The percentage of $L1_0$-MnNi phase in the full concentration range of Fe-Cr-Mn-Ni is presented in Fig. 21(b).

When the region with precipitated $L1_0$-MnNi is compared to the order-disorder transition temperatures, the strong correlation is observed between the percentage of $L1_0$-MnNi in low-temperature phase composition and T_{ODT} of the alloy (Fig. 21(a)): with increasing percentage of $L1_0$-MnNi the T_{ODT} value also increases. This can be interpreted as follows: if the concentration of Mn-Ni is more than 50%, it allows the Mn and Ni atoms to be involved in the formation of $L1_0$-MnNi phase, which is very stable ordered structure. Therefore, even at high temperature, when the other parts of an alloy may become disordered, the $L1_0$-MnNi keeps its order, hence increasing the T_{ODT} value of the composition which it is part of.

D. Short-Range Order Parameters

The chemical Short-Range Order in the system was investigated in detail by analysing the Warren-Cowley SRO parameters, calculated from Eq. A5, derived from Eq. 10, using pair-correlation functions obtained from MC simulations. Inflection points on the Warren-Cowley SRO parameters as functions of temperature indicate the order-disorder transition temperatures, which are the same as the ones obtained from the analysis of mixing enthalpies (see Fig. 22 for exemplary comparisons).

As can be seen from Fig. 22(a,b), the quaternary ground state shows simple behavior - it has one order-disorder transition temperature at 1300 K and all SRO pairs represent the chemical interactions in the quaternary ground state below the T_{ODT}. In the intermetallic phase at 0 K, the Cr atoms do not have Cr neighbors and are surrounded by 2 Fe atoms, 2 Mn atoms, and 8 Ni atoms. Fe and Mn atoms do not have Fe and Mn neighbors and are surrounded by 4 Cr atoms and 8 Ni atoms. Ni atoms are surrounded by 4 Cr, 2 Mn, 2 Fe, and 4 Ni atoms.

Composition of the ORNL sample undergoes two subsequent order-disorder transitions - first at 1320 K, when the $L1_0$-MnNi starts forming, and second at 1180 K, when the $L1_2$ Fe_3Cr starts forming. Those order-disorder transitions are visible both on formation enthalpy as a function of temperature (Fig. 22(c)) and SRO as a function of temperature (Fig. 22(d)). On latter, it is also obvious that the Mn-Ni and Fe-Cr pairs drive the ordering.

The equiatomic composition also undergoes two subsequent order-disorder transition - first at 1140 K, when the $L1_0$-MnNi starts to form, similarly to the ORNL composition. During the second transition at 900 K, the already formed $L1_0$-MnNi phase rapidly dissipates and the environment becomes more uniform, which leads to the gradual formation of the ordered single phase (see Fig. 22(e)). This rapid transformation is also represented by the rapid change of all SRO parameters (Fig. 22(f)).

Comparing the results for ORNL and equiatomic composition, it can be seen that the order-disorder transition is driven by the formation of $L1_0$-MnNi in both alloys and moreover, the behavior of SRO in equiatomic alloy in the intermediate temperature range below the T_{ODT} is similar to that in the ORNL alloy. However, below 900 K the behavior of SRO in two alloys stops being similar. According to the analysis of the nearest neighbors, when the Mn and Ni atoms start to precipitate in the form of the $L1_0$-MnNi, the rest of the composition space in ORNL alloy is close to that of the $L1_2$ Fe_3Cr, the ordered metastable phase (see Fig. S1). This is represented in SRO for ORNL - Mn-Ni and Fe-Cr pairs show attrac-

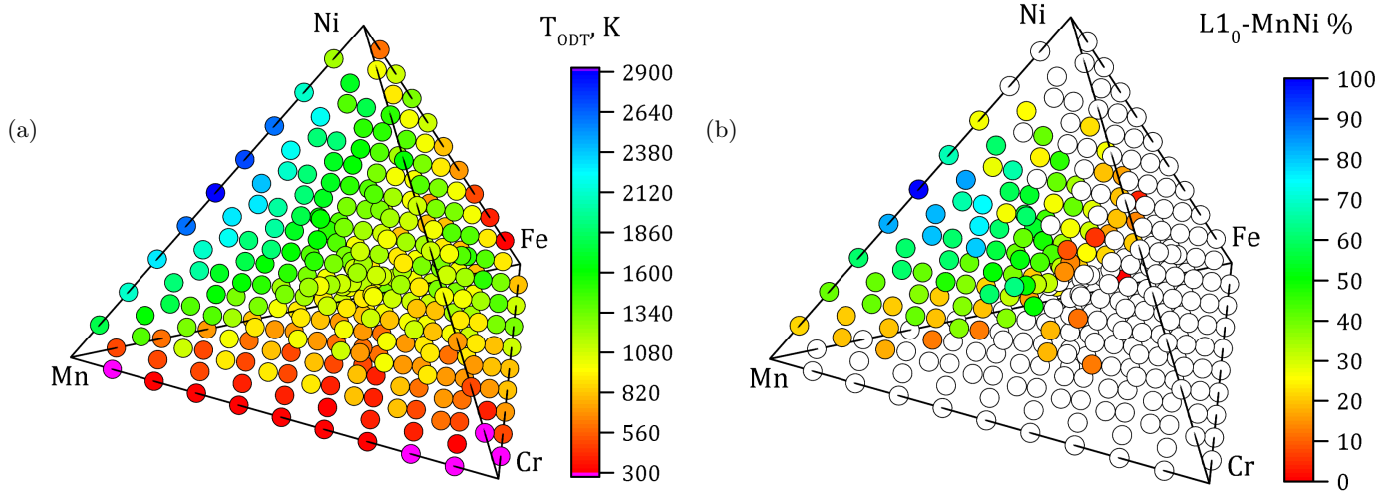

FIG. 21: (a) Order-disorder transition temperatures for whole concentration range of Fe-Cr-Mn-Ni alloy; (b) percentage of AFM $L1_0$-MnNi precipitate at 300 K in the whole concentration range.

tion, and others show repulsion. The situation in the equiatomic alloy is different - the concentration of the Cr and Fe atoms in the alloy part, which is not involved in the formation of $L1_0$ MnNi, are similar. It means that in a contrary to the ORNL alloy there are more Cr atoms which can be attracted by Ni and Mn atoms. As it can be seen in Fig. 22(f), the SRO parameters for Cr-Ni and Cr-Mn pairs are negative for the equiatomic composition, as opposed to the ORNL alloy.

The difference in the SRO for ORNL and equiatomic alloys is most significant at low temperature, but it is noticeable even above the T_{ODT}. It means that most likely, the experimentally obtained alloys will have different properties to some extent. Hence, the extrapolation of the properties of equiatomic alloy, as has been done in Ref.[11], might not be accurate. Also, the influence of SRO on the defect properties, as the extension of the current work, may be of interest.

SRO obtained from MC simulations have been compared to experimental data for four alloy compositions: $Fe_{56}Cr_{21}Ni_{23}$, $Fe_{42.5}Cr_{7.5}Ni_{50}$, $Fe_{38}Cr_{14}Ni_{48}$, $Fe_{34}Cr_{20}Ni_{36}$ (see Supplementary materials, Fig. S 10). Current results reproduce the previous simulations results[21] and are close to experimental values above 1000 K[115,116].

Analysis of the SRO parameters has been conducted for all previously mentioned pseudobinaries, studied with MC, and the results are presented in Supplementary materials, Section S II.

V. CONCLUSIONS

Stability of the quaternary Fe-Cr-Mn-Ni system and all underlying subsystems have been investigated in terms of enthalpies of mixing and enthalpies of formation using the Density Functional Theory (DFT). True fcc Ground States (GSs) have been found in binary and ternary subsystems containing nickel, and their existence is supported by the results of experiments and simulations found in the literature. The fcc quaternary GS $FeCr_2MnNi_4$, which was not previously described in the literature, is predicted to have a negative formation enthalpy at 0 K.

The study of magnetic ordering in the whole concentration range has shown to be consistent with the existing experimental data. The results of simulations allowed to construct the magnetic phase diagram for fcc Fe-Cr-Mn-Ni system. The analysis of volumes and Average Magnitude of Magnetic Moments (AMMMs) in the studied structures with the valence electron concentration larger than 6.97 has shown that the volume per atom correlates with the value of AMMM in a way that the higher values of AMMM correspond to the bigger volumes per atom.

Analysis of the configurational entropy has shown that its influence is the most prominent in the intermediate temperature region, where the order-disorder transition occurs.

Analysis of the SRO parameters has indicated that the interaction between the two elements in the multi-component system is not their intrinsic property, but may vary, sometimes even to the point of inversion, with the change of the concentration in the system. Even the compositions with close concentration of constituting elements, like $Cr_{18}Fe_{27}Mn_{27}Ni_{28}$ and equiatomic CrFeMnNi, show different behavior of SRO parameters, resulting in different microstructure at low temperatures.

The antiferromagnetic $L1_0$-MnNi has been found to be the most stable ordered structure in the multi-component Fe-Cr-Mn-Ni system. The correlation has been indicated between the percentage of $L1_0$-MnNi, precipitated at low temperature, and T_{ODT}.

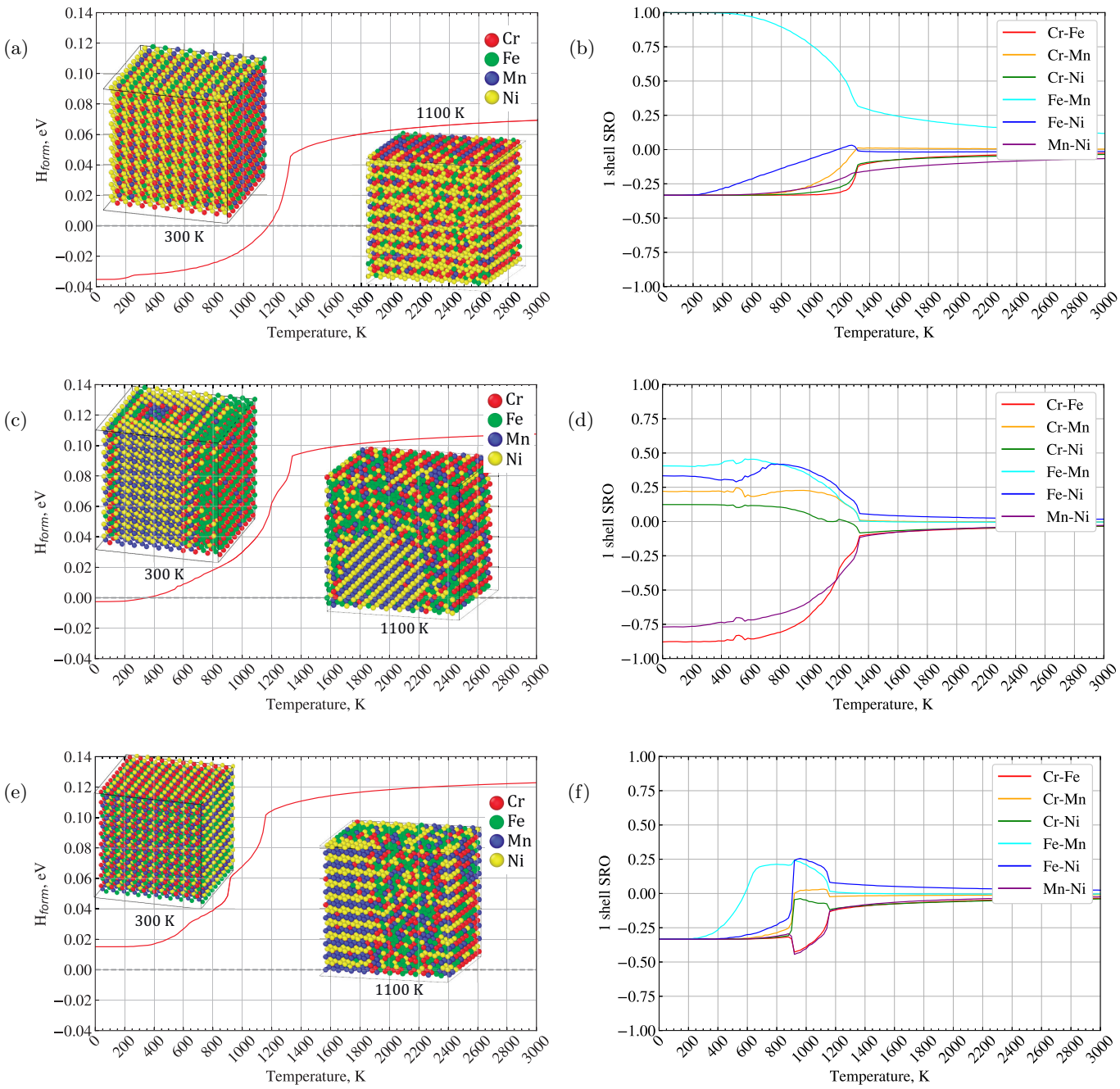

FIG. 22: Formation enthalpy obtained from the MC simulations and the SRO parameters in the first coordination shell for the $FeCr_2MnNi_4$ intermetallic phase (a, b), $Cr_{18}Fe_{27}Mn_{27}Ni_{28}$ [8] (c, d) and the equiatomic composition (e, f). The representative structures of each alloy generated in MC simulations at 300 K and 1100 K are shown inside the figures.

T_{ODT} of the system decreases with decreasing Ni concentration - and the effect is the opposite for the other constituting elements. The AMMMs of all the elements in the alloy increase the most with the increase of Ni content, although the AMMM of Ni is the lowest of all constituting elements. These effects can be of interest because they allow to manipulate the stability and properties of Fe-Cr-Mn-Ni alloys.

As the continuation of the current work, the behavior under irradiation and the defect properties of equiatomic and near-equiatomic Fe-Cr-Mn-Ni alloys will be studied, focusing on the magneto-volume effect, and the Short-Range Order influence on the defect migration.

VI. ACKNOWLEDGEMENTS

MF and JSW acknowledge the financial support from the Foundation of Polish Science Grant HOMING (No. Homing/2016-1/12). The HOMING programme is co-financed by the European Union under the European Regional Development Fund. The simulations were partially carried out with the support of the Interdisciplinary Centre for Mathematical and Computational Modelling (ICM), University of Warsaw, under Grant No. GA69-30. MF would like to thank the UKAEA for its hospitality in CCFE where part of this work has been performed. The work at CCFE has been carried out within the framework of the EUROfusion Consortium and has received funding from the Euratom research and training programme 2014-2018 under Grant Agreement No. 633053 and funding from the RCUK Energy Programme [Grant Number EP/P012450/1]. The views and opinions expressed herein do not necessarily reflect those of the European Commission. AFC acknowledges financial support from EPSRC (EP/L01680X/1) through the Materials for Demanding Environments Centre for Doctoral Training. DNM and JSW acknowledge the support from high-performing computing facility MARCONI (Bologna, Italy) provided by EUROfusion. DNM also acknowledges the support from the Institute of Materials (IMS) at Los Almamos (NM, USA) for the IMS Rapid Response 2018 visit to the Los Alamos National Laboratory (LANL). The authors would like to thank Dr. M. Gilbert (UKAEA) for his carefully reading the manuscript before its submission.

Appendix A: Matrix formulation of SRO

Example τ_K matrices for $K = 2, 3, 4$ are defined below.

$$\tau_2 = \begin{pmatrix} 1 & 1 \\ -1 & 1 \end{pmatrix}, \tau_3 = \begin{pmatrix} 1 & 1 & 1 \\ -1 & \frac{1}{2} & \frac{1}{2} \\ 0 & -\frac{\sqrt{3}}{2} & \frac{\sqrt{3}}{2} \end{pmatrix}, \tau_4 = \begin{pmatrix} 1 & 1 & 1 & 1 \\ -1 & 0 & 1 & 0 \\ 0 & -1 & 0 & 1 \\ -1 & 1 & -1 & 1 \end{pmatrix}. \tag{A1}$$

For triplet or 3-body, the probability-temperature data is generated in a fashion similar to Eq. (12).

$$y_{3,n}^{ABC} = \sum_s (\tau_K^{-1} \otimes \tau_K^{-1} \otimes \tau_K^{-1})_{ABC,(s)} \langle \Gamma_{3,n}^{(s)} \rangle \tag{A2}$$

For 4-body, the probability expression reads:

$$y_{4,n}^{ABCD} = \sum_s (\tau_K^{-1} \otimes \tau_K^{-1} \otimes \tau_K^{-1} \otimes \tau_K^{-1})_{ABCD,(s)} \langle \Gamma_{4,n}^{(s)} \rangle \tag{A3}$$

The inverse matrix of τ_4 is given explicitly below:

$$\tau_4^{-1} = \frac{1}{4} \begin{pmatrix} 1 & -2 & 0 & -1 \\ 1 & 0 & -2 & 1 \\ 1 & 2 & 0 & -1 \\ 1 & 0 & 2 & 1 \end{pmatrix}. \tag{A4}$$

Warren-Cowley SRO parameters can be also computed via the point and pair correlation functions. For a quaternary alloy, the analytical formulas for SRO parameters are following:

$$\alpha_n^{Fe-Cr} = 1 - \frac{1 - 2(\langle \Gamma_{1,1}^1 \rangle + \langle \Gamma_{1,1}^2 \rangle - 2\langle \Gamma_{2,n}^{12} \rangle + \langle \Gamma_{2,n}^{13} \rangle - \langle \Gamma_{2,n}^{23} \rangle) - \langle \Gamma_{2,n}^{33} \rangle}{(1 - 2\langle \Gamma_{1,1}^1 \rangle - \langle \Gamma_{1,1}^3 \rangle)(1 - 2\langle \Gamma_{1,1}^2 \rangle + \langle \Gamma_{1,1}^3 \rangle)}$$

$$\alpha_n^{Cr-Mn} = 1 - \frac{1 - 2\langle\Gamma^3_{1,1}\rangle - 4\langle\Gamma^{11}_{2,n}\rangle + \langle\Gamma^{33}_{2,n}\rangle}{-4\langle\Gamma^1_{1,1}\rangle^2 + (1 - \langle\Gamma^3_{1,1}\rangle)^2}$$

$$\alpha_n^{Cr-Ni} = 1 - \frac{1 - 2(\langle\Gamma^1_{1,1}\rangle - \langle\Gamma^2_{1,1}\rangle + 2\langle\Gamma^{12}_{2,n}\rangle + \langle\Gamma^{13}_{2,n}\rangle + \langle\Gamma^{23}_{2,n}\rangle) - \langle\Gamma^{33}_{2,n}\rangle}{(1 - 2\langle\Gamma^1_{1,1}\rangle - \langle\Gamma^3_{1,1}\rangle)(1 + 2\langle\Gamma^2_{1,1}\rangle + \langle\Gamma^3_{1,1}\rangle)} \tag{A5}$$

$$\alpha_n^{Fe-Mn} = 1 - \frac{1 + 2(\langle\Gamma^1_{1,1}\rangle - \langle\Gamma^2_{1,1}\rangle - 2\langle\Gamma^{12}_{2,n}\rangle + \langle\Gamma^{13}_{2,n}\rangle + \langle\Gamma^{23}_{2,n}\rangle) - \langle\Gamma^{33}_{2,n}\rangle}{(1 + 2\langle\Gamma^1_{1,1}\rangle - \langle\Gamma^3_{1,1}\rangle)(1 - 2\langle\Gamma^2_{1,1}\rangle + \langle\Gamma^3_{1,1}\rangle)}$$

$$\alpha_n^{Fe-Ni} = 1 - \frac{1 + 2\langle\Gamma^3_{1,1}\rangle - 4\langle\Gamma^{22}_{2,n}\rangle + \langle\Gamma^{33}_{2,n}\rangle}{-4\langle\Gamma^2_{1,1}\rangle^2 + (1 + \langle\Gamma^3_{1,1}\rangle)^2}$$

$$\alpha_n^{Mn-Ni} = 1 - \frac{1 + 2(\langle\Gamma^1_{1,1}\rangle + \langle\Gamma^2_{1,1}\rangle + 2\langle\Gamma^{12}_{2,n}\rangle + \langle\Gamma^{13}_{2,n}\rangle - \langle\Gamma^{23}_{2,n}\rangle) - \langle\Gamma^{33}_{2,n}\rangle}{(1 + 2\langle\Gamma^1_{1,1}\rangle - \langle\Gamma^3_{1,1}\rangle)(1 + 2\langle\Gamma^2_{1,1}\rangle + \langle\Gamma^3_{1,1}\rangle)}$$

* markfedorov93@gmail.com
† Corresponding author: jan.wrobel@pw.edu.pl
‡ Corresponding author: duc.nguyen@ukaea.uk

[1] B. Cantor, I. T. H. Chang, P. Knight, and A. J. B. Vincent, Mat. Sci. Eng. A **375-377**, 213 (2004).
[2] D. B. Miracle and O. N. Senkov, Acta Mater. **122**, 448 (2017).
[3] B. J.-w. Yeh, S.-k. Chen, J.-y. Lin, Su-jien Gan, T.-s. Chin, T.-t. Shun, and C.-h. Tsau, Adv. Eng. Mater. **6**, 299 (2004).
[4] Y. Zhang, S. Guo, C. T. Liu, and X. Yang, High-Entropy Alloys. Fundamentals and application (Springer, Cham, 2016).
[5] Z. Li, S. Zhao, R. O. Ritchie, and M. A. Meyers, Prog. Mater. Sci. **102**, 296 (2018).
[6] A. S. Sharma, S. Yadav, K. Biswas, and B. Basu, Mater. Sci. Eng. R **131**, 1 (2018).
[7] O. El-Atwani, N. Li, M. Li, A. Devaraj, J. K. S. Baldwin, M. M. Schneider, D. Sobieraj, J. S. Wróbel, D. Nguyen-Manh, S. A. Maloy, and E. Martinez, Sci. Adv. **5** (2019), 10.1126/sciadv.aav2002.
[8] N. K. Kumar, C. Li, K. Leonard, H. Bei, and S. Zinkle, Acta Mater. **113**, 230 (2016).
[9] K. Jin, C. Lu, L. Wang, J. Qu, W. Weber, Y. Zhang, and H. Bei, Scr. Mater. **119**, 65 (2016).
[10] C. Lu, L. Niu, N. Chen, K. Jin, T. Yang, P. Xiu, Y. Zhang, F. Gao, H. Bei, S. Shi, M. R. He, I. M. Robertson, W. J. Weber, and L. Wang, Nat. Commun. **7**, 13564 (2016).
[11] C. Li, J. Yin, K. Odbadrakh, B. C. Sales, S. J. Zinkle, G. M. Stocks, and B. D. Wirth, J. Appl. Phys. **125**, 155103 (2019).
[12] Z. Wu and H. Bei, Mat. Sci. Eng. A **640**, 217 (2015).
[13] N. D. Stepanov, D. G. Shaysultanov, M. A. Tikhonovsky, and G. A. Salishchev, Mater. Des. **87**, 60 (2015).
[14] E. J. Pickering, R. Muñoz-Moreno, H. J. Stone, and N. G. Jones, Scr. Mater. **113**, 106 (2016).
[15] N. D. Stepanov, D. G. Shaysultanov, M. S. Ozerov, S. V. Zherebtsov, and G. A. Salishchev, Mater. Lett. **185**, 1 (2016).
[16] F. Otto, A. Dlouhý, K. G. Pradeep, M. Kuběnová, D. Raabe, G. Eggeler, and E. P. George, Acta Mater. **112**, 40 (2016).
[17] G. Bracq, M. Laurent-brocq, L. Perri, J.-M. Joubert, and I. Guillot, Acta Mater. **128**, 327 (2017).
[18] Y. Ikeda, B. Grabowski, and F. Körmann, Mater. Charact. **147**, 464 (2019).
[19] Q. Wu, B. He, T. Song, J. Gao, and S. Shi, Comput. Mater. Sci. **125**, 243 (2016).
[20] J. M. Sanchez, Phys. Rev. B **95**, 4 (2017).
[21] J. S. Wrobel, D. Nguyen-Manh, M. Y. Lavrentiev, M. Muzyk, and S. L. Dudarev, Phys. Rev. B **91**, 024108 (2015).
[22] S. Guo, C. Ng, J. Lu, and C. T. Liu, J. Appl. Phys. **109**, 103505 (2011).
[23] Z. Leong, J. S. Wróbel, S. L. Dudarev, R. Goodall, I. Todd, and D. Nguyen-manh, Sci. Rep. **7**, 39803 (2017).
[24] A. van de Walle and G. Ceder, J. Phase Equilib. **23**, 348 (2002).
[25] A. van de Walle, CALPHAD **33**, 266 (2009).
[26] A. Fernández-Caballero, M. Fedorov, J. S. Wróbel, P. M. Mummery, and D. Nguyen-Manh, Entropy **21**, 68 (2019).
[27] A. Fernández-Caballero, J. S. Wróbel, P. M. Mummery, and D. Nguyen-Manh, J. Phase Equilib. Diff. **38**, 391 (2017).
[28] I. Toda-Caraballo, J. S. Wróbel, D. Nguyen-Manh, P. Pérez, and P. E. J. Rivera-Díaz-del Castillo, JOM **69**, 2137 (2017).
[29] D. Ma, B. Grabowski, F. Körmann, J. Neugebauer, and D. Raabe, Acta Mater. **100**, 90 (2015).
[30] A. Van de Walle and G. Ceder, Rev. Mod. Phys. **74**, 11 (2002).
[31] J. A. Barker, Proc. Royal Soc. A **216**, 45 (1953).
[32] G. Kresse and J. Hafner, Phys. Rev. B **47**, 558 (1993).
[33] G. Kresse and J. Hafner, Phys. Rev. B **49**, 14251 (1994).

[34] G. Kresse and J. Furthmüller, Comput. Mater. Sci. **6**, 15 (1996).
[35] G. Kresse and J. Furthmüller, Phys. Rev. B **54**, 11169 (1996).
[36] P. E. Blöchl, Phys. Rev. B **50**, 17953 (1994).
[37] G. Kresse and D. Joubert, Phys. Rev. B **59**, 1758 (1999).
[38] J. P. Perdew, K. Burke, and M. Ernzerhof, Phys. Rev. Lett. **77**, 3865 (1996).
[39] J. D. Pack and H. J. Monkhorst, Phys. Rev. B **13**, 5188 (1976).
[40] A. van de Walle and M. Asta, Model. Simul. Mater. Sci. Eng. A **10**, 521 (2002).
[41] G. L. Hart and R. W. Forcade, Phys. Rev. B **77**, 224115 (2008).
[42] S. V. Barabash, V. Blum, S. Müller, and A. Zunger, Phys. Rev. B **74**, 035108 (2006).
[43] G. Ceder, G. D. Garbulsky, D. Avis, and K. Fukuda, Phys. Rev. B **49**, 1 (1994).
[44] J. W. Connolly and A. R. Williams, Phys. Rev. B **27**, 5169 (1983).
[45] E. Wohlfarth, Handbook of Ferromagnetic Materials, Vol. 1 (Elsevier B.V., 1980) pp. 1–70.
[46] M. Steinitz, J. Magn. Magn. Mater. **60**, 137 (1986).
[47] D. Hobbs, J. Hafner, and D. Spišák, Phys. Rev. B **68**, 14407 (2003).
[48] C. G. Shull and M. K. Wilkinson, Rev. Mod. Phys. **25**, 100 (1953).
[49] J. Hafner and D. Hobbs, Phys. Rev. B **68**, 014408 (2003).
[50] A. C. Lawson, A. C. Larson, M. C. Aronson, S. Johnson, Z. Fisk, P. C. Canfield, J. D. Thompson, and R. B. Von Dreele, J. Appl. Phys. **76**, 7049 (1994).
[51] T. Asada, J. Magn. Magn. Mater. **140-144**, 47 (1995).
[52] G. D. Preston, Philos. Mag. **5**, 1207 (1928).
[53] V. Sliwko, P. Mohn, and K. Schwarz, J. Phys. Condens. Matter **6**, 6557 (1994).
[54] R. W. G. Wyckoff, ed., Crystal Structure (Wiley, 1963).
[55] T. Asada and K. Terakura, Phys. Rev. B **47**, 15992 (1993).
[56] N. Kunitomi, T. Yamada, Y. Nakai, and Y. Fujii, J. Appl. Phys. **40**, 1265 (1969).
[57] J. A. Oberteuffer, J. A. Marcus, L. H. Schwartz, and G. P. Felcher, Phys. Lett. **28**, 267 (1968).
[58] J. Kasper and B. Roberts, Phys. Rev. **101**, 537 (1956).
[59] V. T. Witusiewicz, F. Sommer, and E. J. Mittemeijer, J. Phase Equilib. Diff. **25**, 346 (2004).
[60] S. Lintzen, J. von Appen, B. Hallstedt, and R. Dronskowski, J. Alloys Compd. **577**, 370 (2013).
[61] V. T. Witusiewicz, F. Sommer, and E. J. Mittemeijer, Metall. Mater. Trans. B **34**, 209 (2003).
[62] Y. Yang, Z. Shen, L. Liu, Y. Zhang, C. Song, and Q. Zhai, TMS2015 Supplemental Proceedings **18**, 1457 (2015).
[63] J. Chen and W.-n. Zhang, Mater. Sci. Tech. **34**, 63 (2018).
[64] X. Liang, Structure and Mechanical Properties of Fe-Mn Alloys, Master's thesis, McMaster University (2008).
[65] S. Ruiz-Gómez, R. Ranchal, M. Abuín, A. M. Aragón, V. Velasco, P. Marín, A. Mascaraque, and L. Pérez, Phys. Chem. Chem. Phys. **18**, 8212 (2016).
[66] Y. Ishikawa and Y. Endoh, J. Appl. Phys. **39**, 1318 (1968).
[67] C. Kimball, W. D. Gerber, and A. Arrott, J. Appl. Phys. **34**, 1046 (1963).
[68] R. Kubitz and F. H. Hayes, Monatsh. Chem. **118**, 31 (1987).
[69] M. Huang, P. F. Ladwig, and Y. Austin Chang, Thin Solid Films **478**, 137 (2005).
[70] V. G. Pushin, N. N. Kuranova, E. B. Marchenkova, E. S. Belosludtseva, V. A. Kazantsev, and N. I. Kourov, Tech. Phys.+ **58**, 878 (2013).
[71] C. Guo and Z. Du, Intermetallics **13**, 525 (2005).
[72] N. A. Gokcen, J. Phase Equilib. **12**, 313 (1991).
[73] N. Honda, Y. Tanji, and Y. Nakagawa, J. Phys. Soc. Jpn. **41**, 1931 (1976).
[74] W. B. Pearson, K. Brun, and A. Kjerkshus, Acta Chem. Scand. **19**, 477 (1965).
[75] E. Krén, E. Nagy, I. Nagy, L. Pál, and P. Szabó, J. Phys. Chem. Solids **29**, 101 (1968).
[76] C. Petrillo, F. Sacchetti, and M. Scafi, J. Magn. Magn. Mater. **104–107**, 2015 (1992).
[77] A. Paoletti and F. P. Ricci, J. Appl. Phys. **34**, 1571 (1963).
[78] C. G. Shull and M. K. Wilkinson, Phys. Rev. **97**, 304 (1955).
[79] F. Kajzar and A. Delapalme, J. Magn. Magn. Mater. **14**, 139 (1979).
[80] J. S. Kasper and J. S. Kouvel, J. Phys. Chem. Solids **11**, 231 (1959).
[81] J. Cable and Y. Tsunoda, J. Magn. Magn. Mater. **140-144**, 93 (1995).
[82] D. Spisák and J. Hafner, J. Phys. Condens. Matter **11**, 6359– (1999).
[83] H. Tange, T. Tokunaga, and M. Goto, J. Phys. Soc. Jpn. **45**, 105 (1978).
[84] B. Shanina and V. G. Gavriljuk, Mater. Sci. Forum **638-642**, 3015 (2010).
[85] M. Takahashi, A. Kumar Das, T. Sembiring, H. Iwasaki, and K. Ohshima, Physica B **385-386**, 130 (2006).
[86] M. Takahashi, E. Ahmed, A. Kumar, and Y. Fujii, J. Alloys Compd. **453**, 75 (2008).
[87] A. B. Ziya, M. Takahashi, and K. Ohshima, J. Alloys Compd. **479**, 60 (2009).
[88] H. Sugimura, Y. Kaneno, and T. Takasugi, Mater. Trans. **52**, 1569 (2011).
[89] J. Vrestál, "Landolt-börnstein - group iv physical chemistry," (Springer-Verlag, 2008) Chap. CrFeMn Iron Systems, Part 4.
[90] Y. Matsumot and K. Koyama, ISIJ Int. **30**, 927 (1990).
[91] J. Kouvel, J. Phys. Chem. Solids **16**, 152 (1960).
[92] J. Kouvel and J. Kasper, J. Phys. Chem. Solids **24**, 529 (1963).
[93] J. Singh and C. Wayman, Mater. Sci. Eng. **94**, 233 (1987).
[94] Y.-U. Heo, M. Kim, and H.-C. Lee, Acta Mater. **56**, 1306 (2008).
[95] A. Z. Menshikov, V. A. Kazantsev, and N. N. Kuzmin, JETP Lett. **23**, 6 (1976).
[96] E. F. Wassermann, Phys. Scr. **T25**, 209 (1989).
[97] H. H. Ettwig and W. Pepperhoff, Phys. Status Solidi A **23**, 105 (1974).
[98] A. Menshikov, P. Burlet, A. Chamberod, and J. Tholence, Solid State Commun. **39**, 1093 (1981).
[99] T. Shimura and A. I. S. Kemp, Am. Mineral. **100**, 2545 (2015).
[100] C. Cucciniello, Period. Mineral. **85**, 115 (2016).
[101] S. Hossein Nedjad, S. Meimandi, A. Mahmoudi, T. Abedi, S. Yazdani, H. Shirazi, and M. Nili Ahmadabadi, Mater. Sci. Eng. A **501**, 182 (2009).
[102] D. Geissler, K. H. Müller, J. Freudenberger, K. Nenkov, M. Krautz, J. Eickemeyer, and L. Schultz, J. Alloys Compd. **509**, 3726 (2011).
[103] P. Ehrhart, P. Jung, H. Schultz, and H. Ullmaier, Atomic Defects in Metals, Vol. III/25 (Springer-Verlag Berlin Heidelberg, 1991).

[104] Y. Takano and S. Chikazumi, Kobayashi Rigaku Kenkyusho Hokoku **9**, 12 (1959).
[105] E. A. Owen, E. L. Yates, and A. H. Sully, Proc. Phys. Soc. **49**, 315 (1937).
[106] R. A. Reck and D. L. Fry, Phys. Rev. **184**, 492 (1969).
[107] R. J. Wakelin and E. L. Yates, Proc. Phys. Soc. **66**, 221 (1953).
[108] M. L. Bhatia, A. K. Singh, and T. K. Nandy, **4**, 635 (1996).
[109] A. G. Schlijper and B. Smit, J. Stat. Phys. **56**, 247 (1989).
[110] L. G. Ferreira, C. Wolverton, and A. Zunger, J. Chem. Phys. **108**, 2912 (1998).
[111] R. Kikuchi, Phys. Rev. **81**, 988 (1951).
[112] M. Lavrentiev, S. L. Dudarev, and D. Nguyen-Manh, J. Nucl. Mater. **386-388**, 22 (2009).
[113] M. E. J. Newman and G. T. Barkema, eds., Monte Carlo Methods in Statistical Physics (Clarendon Press, 1999).
[114] G. Federici, W. Biel, M. R. Gilbert, R. Kemp, N. Taylor, and R. Wenninger, Nucl. Fusion **57**, 092002 (2017).
[115] P. Cenedese, F. Bley, and S. Lefebvre, Acta Crystallogr. A **40**, 228 (1984).
[116] A. Z. Menshikov, C. Dimitrov, and A. E. Teplykh, J. Phys. III **7**, 1899 (1997).